ABSTRACT

Title of Dissertation: MEASUREMENT OF EFFECTIVE CURE SHRINKAGE OF EPOXY MOLDING COMPOUND AND INDUCED IN-LINE WARPAGE DURING MOLDING PROCESS

Changsu Kim, Doctor of Philosophy, 2023

Dissertation directed by: Professor Bongtae Han
Department of Mechanical Engineering

Cure shrinkage accumulated only after the gel point is known as effective cure shrinkage (ECS), which produces residual stresses inside molded components. The ECS of an epoxy-based molding compound (EMC) is measured by an embedded fiber Bragg grating (FBG) sensor. Under a typical molding condition, a high mold pressure inherently produces large friction between EMC and mold inner surfaces, which hinders EMC from contracting freely during curing. A two-stage curing process is developed to cope with the problem. In the first stage, an FBG sensor is embedded in EMC by a molding process, and the FBG-EMC assembly is separated from the mold at room temperature. The molded specimen is heated to a cure temperature rapidly in the second stage using a constraint-free curing fixture. The ECS of an EMC with a filler content of 88 wt% is measured by the proposed method, and its value is 0.077%.

The measured ECS can be used to predict the warpage caused by molding processes. The validity of the prediction can be verified only by measuring the warpage during molding. A point-based measurement technique utilizing uniquely-generated multiple beams and binarization-based beam tracing method is developed to cope with the challenges associated with the warpage measurement during molding. The proposed method is implemented successfully to measure the warpage of a bimaterial disk that consists of aluminum and EMC as a function of time during molding process. Measurements are repeated to establish the measurement accuracy of the proposed method.

QUANTITATIVE MEASUREMENT OF EFFECTIVE CURE SHRINKAGE OF EPOXY MOLDING COMPOUND AND IN-SITU CHARACTERIZATION OF INDUCED-RESIDUAL DEFORMATIONS

by

Changsu Kim

Dissertation submitted to the Faculty of the Graduate School of the
University of Maryland, College Park, in partial fulfillment
of the requirements for the degree of
Doctor of Philosophy
2023

Advisory Committee:
Professor Bongtae Han, Chair/Advisor
Professor Patrick McCluskey
Professor Peter Sandborn
Dr. Michael Osterman
Professor Sung W. Lee, Dean's Representative

Acknowledgements

Throughout my Ph.D., I got help from so many people. It has been a long and challenging journey. Still, considering the help and learning I have received, it has been invaluable. I want to say thank you to them.

First and foremost, I want to express my deepest gratitude to my advisor, Dr. Bongtae Han. I have learned a tremendous amount of things from him. From start to finish, I couldn't have done this without his dedicated help and guidance. I am so grateful for the lessons that are helpful not only academically but also in life. I will not forget them in my future life.

I would also like to say thank you to my committee members, Dr. Patrick McCluskey, Dr. Peter Sandborn, Dr. Michael Osterman, and Dr. Sung Lee, for serving on my committee and giving me valuable comments during my defense.

I would like to thank my current and former lab mates, Sukrut, Jack, Yongrae, Roshith, Hyun, Bulong, Sean, Altur, and Byung, for their help and support during this journey. I really enjoyed the time discussing and conducting experiments with them.

I want to say thank you to Dr. Ran Tao, Dr. Zhaoyang Wang, Dr. Jooyoung Chung, and Dr. Ki Hyeok Kwon for helping me with my research despite their busy schedules.

Lastly, I want to say a huge thank you to my family and parents. Without their help and support, I really could not have finished this. Thank you to my son, Asher, for giving me happiness and another meaning in life, and thank my wife, Yu Hyun, for understanding, helping, and encouraging me so much.

Table of Contents

List of Figures

Chapter 1: Background

1.1. Epoxy molding compound and effective cure shrinkage

Various thermosetting polymers are used in the semiconductor packages. The polymer changes from the viscous fluid to solid due to the curing. During solidification, each cross-linking causes incremental volumetric shrinkage called "*cure shrinkage*". Cure shrinkage produces curing-induced residual stresses in molded components [1-3]. To generate the residual stress, the modulus of the polymer should be nonzero, and only the cure shrinkage occurred after the modulus becomes nonzero has to be used to predict the residual stress. The modulus is near zero when the polymer is uncured, but the modulus starts evolving after passing its gel point. Therefore, only the cure shrinkage accumulated after the gel point, known as the "*effective cure shrinkage* (ECS)" [4], should be used to determine cure-induced residual stresses. Curing process itself does not generate any stresses, but the residual stress is generated during the curing process when the polymer is constrained by adjacent materials such as chip, substrate, etc.

Epoxy-based molding compounds (EMC) are used widely to house the semiconductor chip and other internal circuitry of electronic packages, in order to provide protections from environments. Such a package is illustrated schematically in Fig. 1(a), where the encapsulation by EMC is achieved by the well-known transfer molding process. EMC is a composite material consisting of epoxy resin as a matrix and silica particles as a filler. EMC typically has a very large filler content (as high as

90 wt%) to attain desired thermomechanical properties. Fig. 1(b) shows a scanning electron microscopy (SEM) image of EMC, where the high filler content is evident.

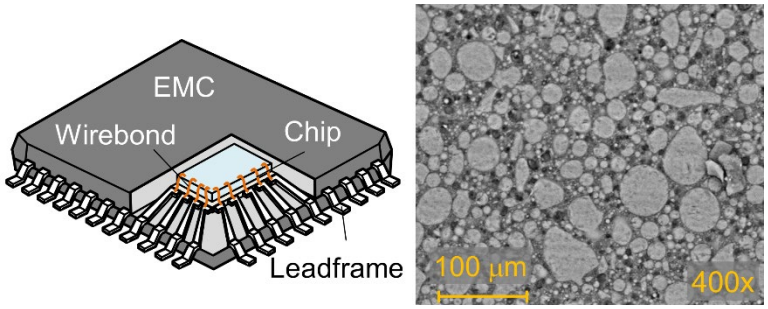

Fig. 1. (a) Schematic diagram of a semiconductor chip encapsulated by EMC, (b) Scanning electron microscopy (SEM) image of typical EMC [5].

The most widely used molding process for electronic packages, known as *transfer molding*, is illustrated schematically in Fig. 2. An EMC pellet is charged in the transfer pot. After heating it to a mold temperature where EMC becomes highly viscous, a ram force is applied to transfer the charge from a transfer pot to cavities containing electronic packages, as shown in (a). The molding compound is driven through narrow channels called "runners", which connect the transfer pot to the gates of cavities. During its transfer, the molding compound remains as a viscous liquid, and thus the mold pressure caused by the ram force is transferred to all cavities, as illustrated in (b). The top mold is separated from the bottom mold for removal of the encapsulated components after curing.

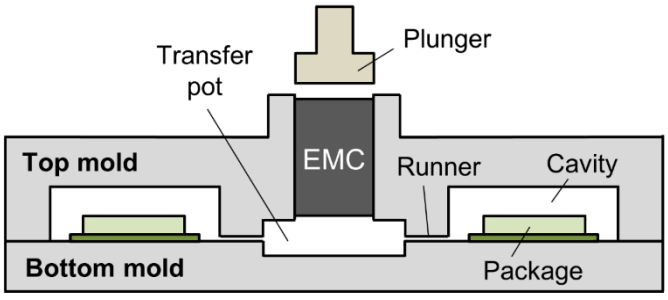

(a)

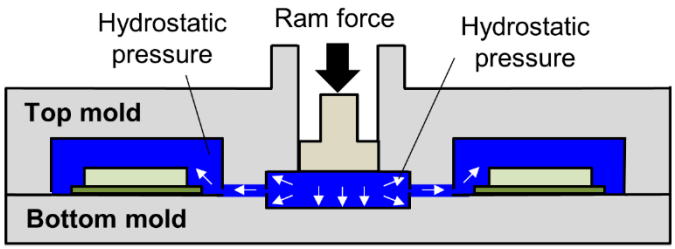

(b)

Fig. 2. Schematic illustration of transfer molding process: (a) EMC is charged, and the mold is heated to the mold temperature; and (b) transfer occurs while EMC remains as a viscous liquid [5].

Another critical quantity that affects the magnitude of cure-induced residual stresses is the modulus at a cure temperature. Curing is typically done at a temperature higher than $T_{g\infty}$ (the glass transition temperature of a fully cured polymer), where the modulus rapidly decreases. The modulus of un-filled or lightly-filled thermosetting polymers is usually very low at curing temperatures, and thus residual stresses caused by ECS may not be significant. However, the modulus of a highly-filled EMC can be as large as 1.5 GPa at a mold temperature, where EMC is transferred and cured [6]. As a result, the residual stresses in molded components, caused by the ECS of EMC, can be very significant at the mold temperature.

Unlike classical methods to measure the *total* cure shrinkage where only a volume change after curing is documented, a technique employed to measure ECS should satisfy two critical requirements: (1) a sensor should be able to measure a stress-induced strain directly during curing since the gel point must be identified accurately; (2) a sensor should be so robust not to be degraded by polymers and/or volatiles as well as harsh curing conditions (temperature, pressure, etc.).

A fiber Bragg grating (FBG) is an optical strain sensor that offers very high sensitivity (≈ 1 microstrain). It is extremely robust, as it is fabricated on a glass fiber. These advantages were exploited to measure the residual stress/strain in composite materials [7], and the ECS values of various materials [4, 8-10].

For the ECS measurement, an FBG sensor is embedded in a specimen, and thus, a mold to contain uncured polymers in a liquid state is required. The most critical challenge encountered during the measurement is to negate the effect of the mold on the ECS.

The ECS of an underfill was measured using the silicone rubber mold in Ref. [10]. The modulus of the silicone rubber mold is very low so that the volume stiffness of the mold is negligibly smaller than that of the polymer. The instantaneous equilibrium modulus and the increment of the effective cure shrinkage were measured for each segment after the gel point, and those were used to calculate the evolution of the ECS. To measure both properties during the curing, two specimens with different configurations were cured simultaneously.

The ECS of a silicone elastomer was measured using a very flexible plastic wrap mold in Ref. [4]. Due to the small modulus of the elastomer, a thin plastic wrap was used as a mold to make the effect of the mold negligible. The mold was deformed very easily, and the room temperature curing was only feasible. It was able to be used because the silicone elastomer can be cured completely at room temperature. The silicone elastomer shows an elastic behavior so that the modulus after the curing and the total cure shrinkage are required for the ECS calculation.

The residual strain of room and high temperature epoxies were measured using flexible nitrile sleeve mold [9, 11]. All the strain after the gel point was assumed to be transferred to the FBG. However, a significant temperature increase was observed due to the large diameter of the specimen. The temperature distribution makes the curing non-uniform. Also, it causes the inaccuracy of the ECS measurement from the BW shift because the BW is changed by both cure shrinkage and temperature change.

There are many types of polymers used in semiconductor packages, and each polymer has different characteristics such as cure kinetics, modulus, T_g and viscosity. Consequently, a single curing setup and procedure cannot be applied to every polymer and the curing setup and procedure should be tailored based on their characteristics.

1.2. Warpage and residual stress

The residual stresses exist inherently in components encapsulated by molding processes. They are combined with the stresses caused by the coefficient of thermal expansion (CTE) mismatch, and eventually dictate the final warpage of components at room and reflow temperatures, which must be controlled for handling and yield during manufacturing.

The warpage evolution of an encapsulated package during manufacturing is illustrated schematically in Fig. 3, where transfer molding is used to encapsulate the package. The package bends upward ($\cup$) at the mold temperature, as illustrated in Fig. 3(a), because a molding compound shrinks during curing. When the package is heated to the reflow temperature after molding, however, the CTE mismatch causes the package to bend downward ($\cap$), as illustrated in Fig. 3(b), because the CTE of a molding compound at the peak reflow temperature is higher than those of adjacent

materials. Obviously, both quantities are required to accurately predict the warpage at the peak reflow temperature.

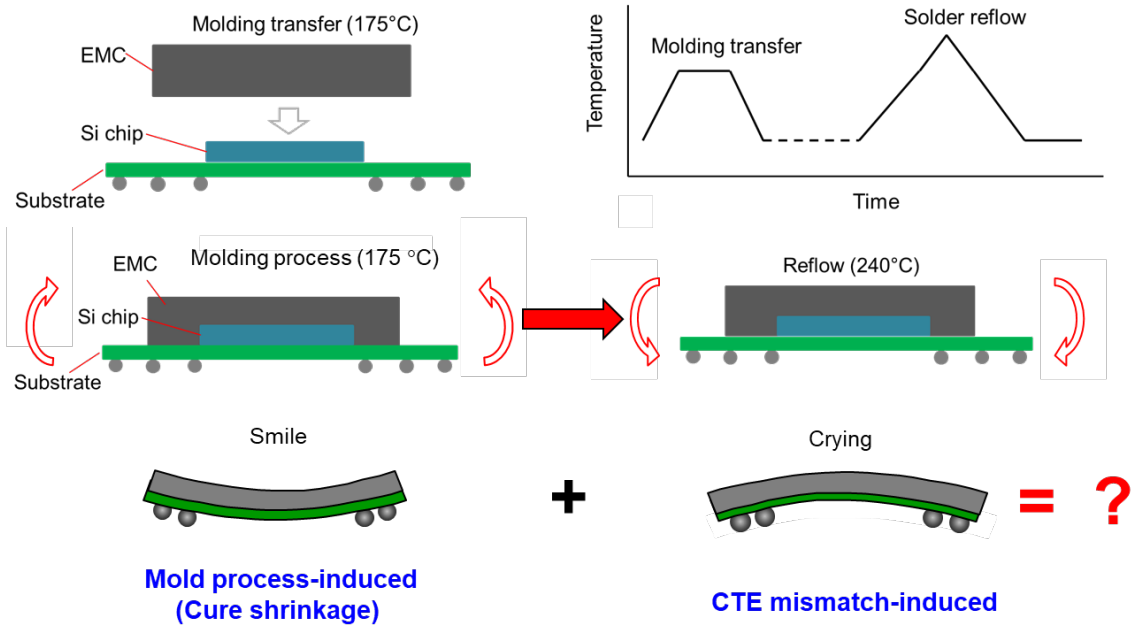

Fig. 3. Illustration of warpage evolution during manufacturing [12].

The original problem definition of warpage involved controlling the warpage of a single component at the solder reflow temperature. The printed circuit board (PCB) was relatively thick, and it was reasonable to assume that the PCB was flat at the reflow temperature considering the symmetric design of signal planes with respect to the center power plane. Thus, the component warpage was controlled simply not to exceed certain specifications (relative to solder ball sizes) and thus to avoid solder bridging or opening during the assembly process, as illustrated in Fig. 4.

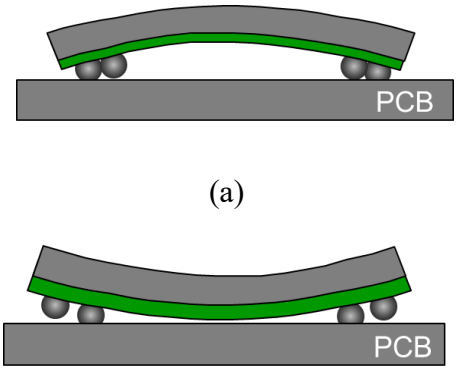

(a)

(b)

Fig. 4. Illustration of (a) solder bridging and (b) solder opening during assembly [13].

The warpage issue became more challenging when the portable electronics industry adopted the package-on-package (PoP) technology. In typical mobile phone applications, a top package (typically low I/O memory module) is stacked on a bottom package (typically high I/O logic module) using solder balls. Naturally, the packaging requirements of the two packages are different (e.g., wire-bond vs. flip-chip), and so are their thermomechanical behaviors, i.e., warpage. In order to accommodate this inherent warpage behavior difference, solutions have to be tailored to account for the system reliability. As illustrated in Fig. 5, the package warpages are allowed only if they are in the same direction.

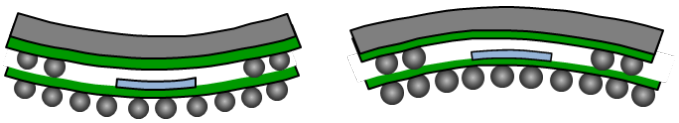

(a)

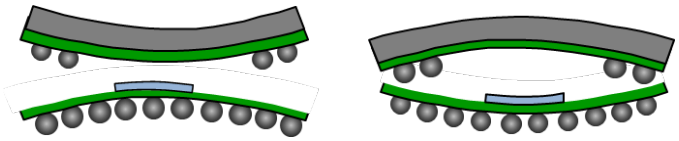

(b)

Fig. 5. Illustration of (a) acceptable and (b) unacceptable warpage combinations [13].

The warpage caused by the EMC molding process can be significant due to the high modulus of EMC. More recently, the warpage issue became even more challenging simply because EMCs became a part of some interconnect systems in various heterogeneous integration solutions, including fan-out wafer level packaging (FO-WLP) and embedded technologies, where vias and signal redistribution layers are fabricated in or on EMC after molding is completed [14-19]. The wafer level warpage of FO-WLP at room temperature is illustrated in Fig. 6, which can be excessive due to a large wafer size. This must be controlled for successful process integration (e.g., fabrication of redistribution layer) after molding is completed.

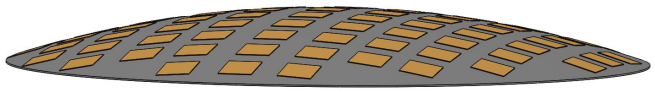

Fig. 6. Illustration of the warpage of FO-WLP wafer at room temperature [13].

1.3. Motivation

A fiber Bragg grating (FBG) sensor has been used to measure the effective cure shrinkage (ECS) or the residual strain [4, 9-11, 20-22]. The generalized plane strain solution used to calculate the ECS is based on the uniform curing of polymer without mechanical constraints. A mold is used to cure the polymer, and the shrinkage of the polymer can be constrained by the mold. Its effect could be significant especially when the modulus of the polymer is small. The curing setup and procedure have to be designed to minimize the effect of the mold on the measurement while considering the characteristics of polymers.

EMC has been used widely for encapsulating the semiconductor packages, a residual stress caused by the ECS could be significant due to the high modulus. The pressure should be applied to the EMC during the molding process, and the specially designed mold and procedure needs to be used. Constraints during the ECS measurement could be very large.

The measurement of the ECS of the EMC by the FBG sensor provides the amount of the ECS, and this could be used for numerical prediction. The accuracy of the prediction could be verified by the measurement of the warpage and residual stress during and after the molding process, but the molding process of the EMC is done inside the mold, and the existing measurement techniques for the warpage cannot be used.

1.4. Objective

The objective is thus 1) to characterize the curing-related properties of EMC during the transfer molding process, 2) to verify the accuracy of numerical models to predict deformations of EMC encapsulated packages. Achieving the objective entails:

(1) To develop a setup and procedure that can eliminate the constraints on the specimen completely during the ECS measurement.

(2) To characterize the ECS of EMC during the molding process.

(3) To measure cure-induced warpage of EMC encapsulated packages generated during the transfer molding process.

1.5. Organization of dissertation

In this study, a novel technique to measure the effective cure shrinkage of the EMC and the warpage generated during the transfer molding process will be developed. In Chapter 2, the ECS measurement of the EMC will be presented. The mold options to minimize the effect of the constraints will be discussed. The measurement technique will be explained, and the determination process of the experimental parameters will be shown. The measurement data and the repeatability of the measurement will be presented.

In Chapter 3, the warpage measurement technique during the transfer molding process will be introduced. The point-based measurement technique is explained first, and the accommodation of the technique for the warpage measurement during the molding process will be discussed. The development process of an optical system,

image processing, and the molding will be presented. Tests to evaluate the accuracy and the uncertainties of the measurement systems will be introduced. Then, the warpage measurement result during the transfer molding process will be presented.

Chapter 4 contains a conclusion of the study, contributions made by this dissertation, and a future works to be extended from this study.

Chapter 2: Effective Cure Shrinkage Measurement of Epoxy Molding Compound

2.1. Technical background

The definition of the effective cure shrinkage is reviewed first. The fundamentals of the FBG-based method to measure the effective cure shrinkage are followed. The chemical and diffusion controlled curing process are reviewed.

2.1.1 Effective cure shrinkage (ECS)

The behavior of a typical polymer system during curing is illustrated in Fig. 7 [8], where the *x*-axis shows an arbitrary time scale, and the *y*-axis represents two polymer properties associated with curing (cure shrinkage, $\varepsilon(t)$, and modulus, $E(t)$), normalized by their final values, ε_∞ and E_∞, obtained at full-cure [10]. The cure shrinkage is proportional to the extent of cure, and the modulus evolves non-linearly with time.

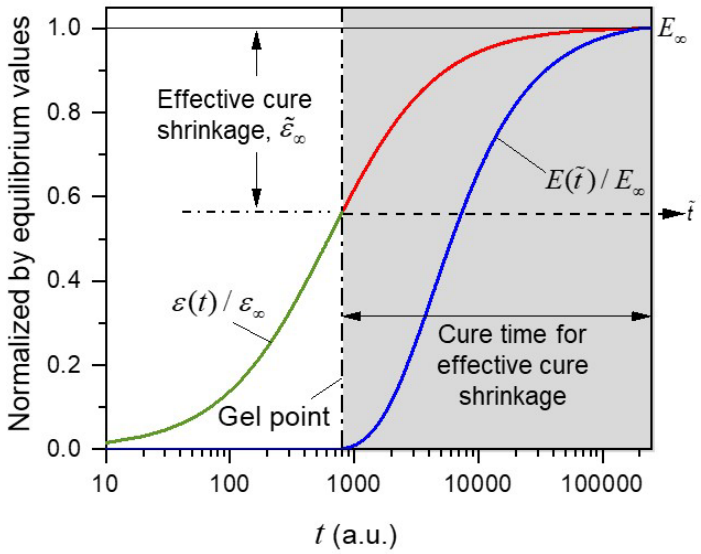

Fig. 7. Schematic illustration of cure shrinkage and modulus evolution during curing [5].

As mentioned earlier, cure shrinkage does occur before the gel point (denoted as t_{gel}), but the modulus associated with the cure shrinkage developed before t_{gel} is virtually "zero". In the figure, the time after t_{gel} and the effective cure shrinkage are denoted as $\tilde{t}$ and $\tilde{\varepsilon}(\tilde{t})$, respectively. It is important to note that the moment at which gelation occurs must be precisely identified in order to measure the ECS quantity accurately.

2.1.2 FBG-based method

A fiber Bragg grating (FBG) reflects a narrow band of wavelengths of light while transmitting other wavelengths. It is achieved by creating a periodic variation in the refractive index of an optical fiber [23]. The center of the reflected wavelength is called Bragg wavelength (BW), which is defined as:

$$\lambda_B = 2n_{eff}\Lambda \tag{1}$$

where λ_B is BW; n_{eff} is the effective refractive index; and Λ is the grating pitch.

In the method, an FBG sensor is embedded in a cylindrically shaped uncured polymer. As illustrated in Fig. 8, the polymer shrinks around the FBG sensor as curing progresses. After the gel point, the effective cure shrinkage of the polymer starts to deform the FBG sensor, and the BW shift is resulted.

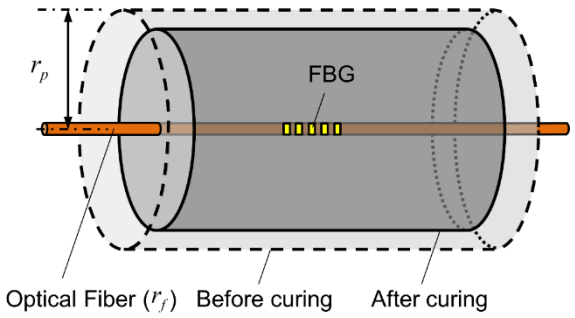

Fig. 8. Schematic illustration of a specimen configuration with an embedded FBG sensor [5].

The generalized plane strain solution for the stress components of the FBG sensor, caused by the effective cure shrinkage, was first derived by Wang et al. [24]. It was later utilized to define the relationship between the BW shifts and the effective cure shrinkage [4, 8, 10]. The relationship can take a form of

$$\tilde{\epsilon}_\infty = \frac{\Delta\lambda_B}{\lambda_B}\left[F(E_f, E_p, \beta)\right]^{-1} \tag{2}$$

where $\tilde{\epsilon}_\infty$ is the linear effective cure shrinkage; $\Delta\lambda_B$ is the BW shift measured during curing; E_f and E_p are the moduli of the fiber and the polymer, respectively; $\beta = \frac{r_p}{r_f}$ is called "configuration", where r_f and r_p are the radii of the fiber and the polymer, respectively; and $F()$ is a nonlinear function, which can be expressed explicitly. The

effective cure shrinkage can be determined from $\Delta\lambda_B$ when the Poisson's ratio and the modulus of the polymer are known [8, 10].

It was also shown in Ref. [24] that the curing-induced radial stress of the fiber is much smaller than the corresponding axial stress, which makes the loading condition of the FBG sensor virtually uniaxial. Under this condition, Eq. (2) is reduced to [24]:

$$\tilde{\epsilon}_\infty = \frac{\Delta\lambda_B}{\lambda_B(1-P_k)} \cdot \zeta(E_p, \beta) \tag{3}$$

where P_k is the equivalent strain-optic constant [23], and ζ is the strain-transfer ratio, which is defined as $\frac{\epsilon_f}{\tilde{\epsilon}_\infty}$ where ϵ_f is the axial strain of the fiber caused by the effective cure shrinkage.

The strain-transfer ratio is strongly dependent on the volume stiffness ratio between the polymer and the fiber. The volume stiffness ratio, $\hat{R}_{VS}$, can be defined as [25]:

$$\hat{R}_{VS} = \frac{E_p\left(r_p^2 - r_f^2\right)}{E_f \cdot r_f^2} \tag{4}$$

The value of ζ converges to "unity" when the volume stiffness ratio approaches a large value. Under this condition (defined as "infinite configuration" in Ref. [25]), the effective cure shrinkage of a polymer is fully transferred to the fiber regardless of the polymer's modulus.

2.1.3 Chemical and diffusion control

During the curing process, thermosetting polymers are solidified through a chemical reaction that causes polymer chains to cross-link. The general form of a curing rate can be expressed as:

$$\frac{dp}{dt} = k_c(T,p)\phi(p) \tag{5}$$

where p is the extent of cure (or cure-extent); k_c is a temperature and cure dependent rate coefficient; and $\phi(p)$ is the cure kinetic function that can take any mathematical form of p.

When the reaction is controlled by the kinetics of the chemical reaction, it is called "chemical control" [26]. T_g increases from T_{g0} to $T_{g\infty}$ as a function of extent of cure. When a polymer is cured at the temperature lower than T_g, the mobility of the chains is constrained, and the rate of cure slows down significantly when the T_g becomes to T_{cure} [27]. The polymer will transit from a liquid or rubbery to a glass state, and it is called vitrification [26, 27]. The reaction rate slows down significantly during vitrification because the reaction becomes diffusion-controlled [27-29]. When the rate of cure is decreased by the diffusion control, the kinetic rate equation should be corrected by a factor describing the effects of the rate change.

$$\left(\frac{dp}{dt}\right)_{DF} = k_c(T,p)\phi(p)\cdot DF(T,p) \tag{6}$$

where $\left(dp/dt\right)_{DF}$ is the rate of cure in diffusion controlled condition, DF is the diffusion factor correcting the rate of cure in chemically controlled condition [26]. In result, the absence of mobility makes the final conversion lower than unity [26].

When the ECS of the thermosetting polymer is measured, T_{cure} should be higher than $T_{g\infty}$ if the total ECS value of fully cured polymer is desired. However, the measurement of the ECS of some polymers at the temperature above $T_{g\infty}$ can be very challenging if the rate of cure at the temperature near $T_{g\infty}$ is too fast. If the polymer passes the gel point before the specimen temperature reaches T_{cure}, an accurate ECS measurement cannot be done because the BW change is affected by both temperature change and the effective cure shrinkage.

2.2. Mold options

The ECS is calculated from the BW shift, and the generalized plane strain solution is based on no external mechanical constraints on the polymer. In actual curing measurements, achieving this condition is challenging because the mold is required to contain uncured polymers in a liquid state as mentioned above. When cure shrinkage of the polymer occurs, the mechanical constraints on the polymer can be generated by the mold. This effect should be minimized in the ECS measurements. To do that, the mold and curing procedures should be designed to minimize the constraints to the polymer during the ECS measurement. Because each polymer has different mechanical properties, a single design of the mold cannot be used for measuring ECS of all polymers. The following three mold options are suggested to be used for the ECS measurement.

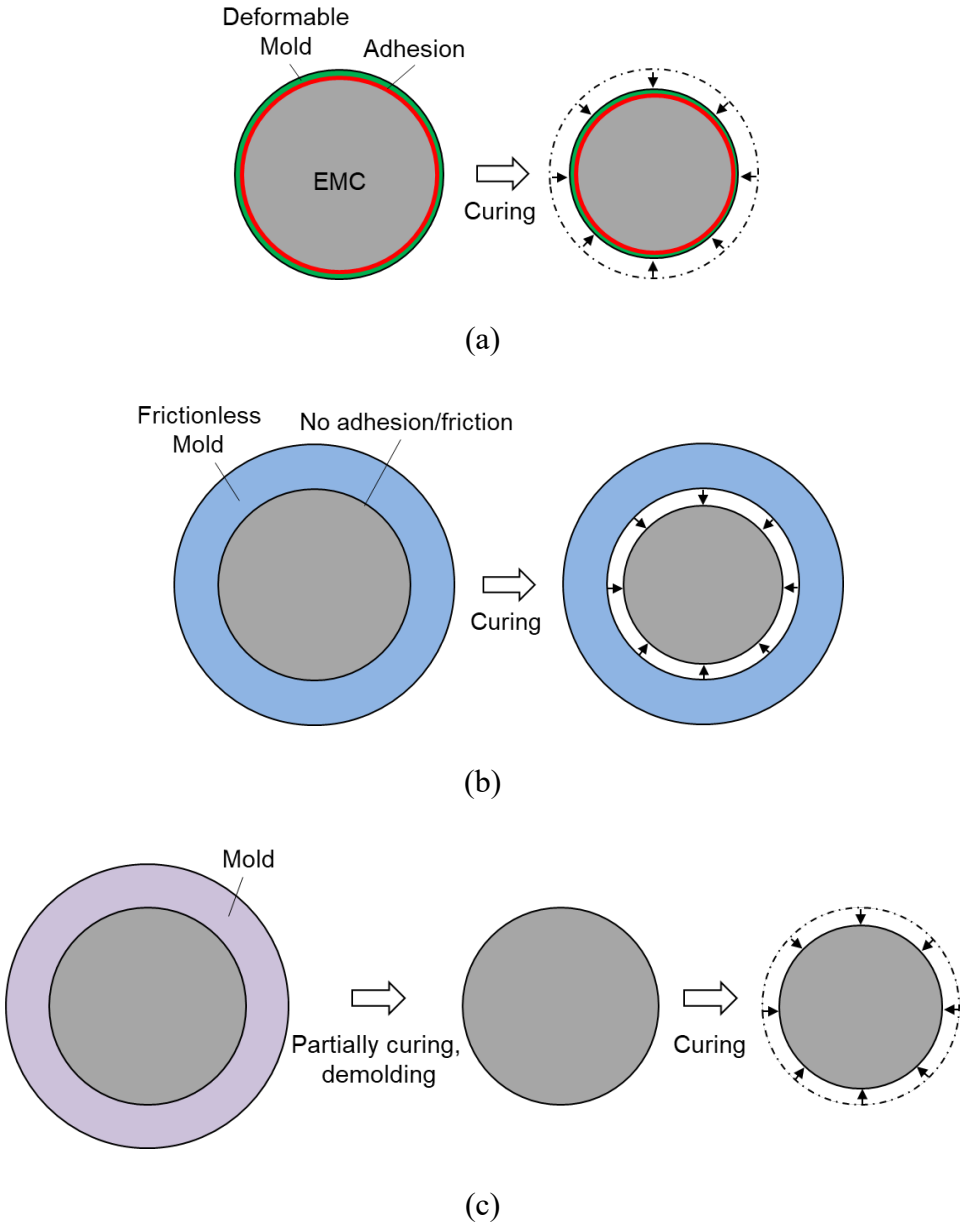

Fig. 9. Schematic illustration of cross-sectional view of three mold options, (a) deformable mold, (b) frictionless mold, (c) two-stage curing process.

First, the mold can be fabricated with a very soft material so that it can deform together with the polymer. materials with a very low modulus material can be used for a mold to minimize the volume stiffness of the mold. The mold material should be checked whether the polymer adheres to the mold so that the mold can deform together with the polymer. This type of mold was used for the ECS measurement of the silicone

elastomer [4]. A very thin and flexible plastic wrap used as a mold, and it deformed with the elastomer during the curing.

Second, the mold can be frictionless, and the polymer shrinks without constraints. The friction between the mold and the specimen should be negligible, and the specimen is supposed to shrink with negligible constraints. The polymer should not adhere to the mold, and the length of the specimen is important because the polymer far from the center should move more, and the effect of friction will be larger.

Third, two-stage curing process can be used. A polymer can be partially cured, separated from the mold, and cured in a completely constraint-free condition. When the temperature of the specimen is lower than the T_g of the polymer, the polymer vitrifies and becomes glassy even though it did not pass the gel point. The shape of the specimen is made using a mold in the stage I. The temperature does not need to be as high as T_{cure}, but large enough to make the polymer viscous liquid and change its shape. The mold can be cooled down lower than T_g of the partially cured polymer, and the specimen can be separated. The specimen now can be heated to T_{cure} without using the mold. The extent of cure after the stage I can be low, but the viscosity of the specimen at T_{cure} should be large enough to maintain its shape. Often the specimen has to be heated quickly to T_{cure} to avoid passing the gel point when the temperature of the specimen stabilizes.

2.3. ECS measurement of EMC

The ECS of EMC has not been characterized quantitatively because of testing complexity associated with a high mold temperature and a high mold pressure. As

mentioned earlier, however, the EMC molding condition requires the high temperature and pressure, and thus a rigid metal mold must be used to accommodate the condition. Under this condition, large friction between EMC and mold inner surfaces would occur, which would also hinder EMC from contracting freely during curing. In this section, a novel two-stage curing process is developed to provide a constraint-free curing condition for EMC. A specimen with an infinite configuration is used to measure the ECS.

2.3.1 Two-stage curing for constraint-free measurement

A two-stage curing process is developed to cope with the problem associated with friction caused by the mold pressure. A history of temperature and pressure during the proposed two-stage curing process is illustrated in Fig. 10. Prior to Stage I, a small hole (slightly larger than the fiber diameter) is drilled along the center of a preformed EMC pellet to accommodate the optical fiber. In Stage I, the EMC and FBG subassembly is heated slowly to a mold temperature, T_{mold}, ($a - b$), and a mold pressure is applied at T_{mold} (b). After the pellet is collapsed into a metal mold (b), the mold pressure is removed at (c), and the mold is cooled down to room temperature (d). The molded EMC specimen with the embedded fiber is separated from the mold at room temperature ($d - e$).

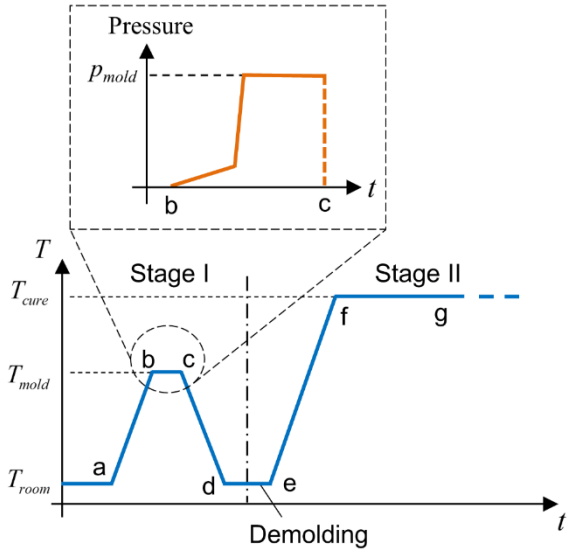

Fig. 10. Schematic illustration of two-stage curing process. Stage I: (a-b) heating to T_{mold}; (b) pressure application; (c) removal of pressure and cooling down to T_{room}; and (d) demolding at T_{room}. Stage II: (e-f) heating to T_{cure}; (f-g) temperature stabilization at T_{cure}; and (g–) curing [5].

The inset of Fig. 10 shows how the pressure is applied at T_{mold}. It is suggested that a small amount of pressure be applied slowly first to collapse the pellet, and then the rest of mold pressure (p_{mold}) be applied quickly. This procedure of pressure application minimizes the lateral movement of the fiber while collapsing the pellet. It is important to note that T_{mold} should be only slightly higher than T_g of the uncured EMC so that the pellet can deform under the mold pressure while minimizing the amount of curing.

In Stage II, the EMC specimen prepared in Stage I is heated to a cure temperature, T_{cure} ($e-f$), and is continuously cured until no change in the BW shift is observed (g). The most critical requirement for Stage II is that the EMC specimen should not reach its gel point before the specimen reaches T_{cure}. (f). It is to be noted that the BW change at a constant temperature occurs only when a fiber is subjected to

a mechanical strain. This critical feature is to be exploited to identify the gel point during curing ($f-g$).

Several technical considerations are to be given to determine a proper specimen configuration, β, and a cure temperature, T_{cure}. The configuration will have to be determined first. It is clear from Eq. (4) that the volume stiffness ratio, $\hat{R}_{VS}$, and thus the strain transfer ratio, ζ, increases as the EMC radius (i.e., β) does. However, the maximum configuration is limited in practice due to heat generation during curing. If heat generation produces a large temperature gradient within a specimen, the accuracy of ECS measurement can be affected significantly [10]. In general, the requirement of the infinite configuration sets the lower bound of β while a condition for uniform curing does the upper bound.

As mentioned earlier, the value of T_{cure} should be chosen carefully so that that the EMC specimen at T_{cure} does not pass the gel point. This sets the maximum value of T_{cure}. The minimum value of T_{cure} should be greater than $T_{g\infty}$ (the glass transition temperature of a fully-cured EMC). It is well known that T_g of polymer increases as the extent of cure increases. If T_{cure} is lower than $T_{g\infty}$, a phenomenon known as vitrification will occur when the glass transition temperature of a partially cured EMC reaches T_{cure} [27, 29].

2.3.2 Specimen configuration and cure temperature

An epoxy-based molding compound with a filler content of 88 wt% was tested. The lower bound of the configuration was estimated first by considering the strain-

transfer ratio, ζ. The E and β combinations that offer the infinite configuration (i.e., $\zeta > 0.99$) are shown in Fig. 11 (green solid line). The temperature-dependent moduli reported in Ref. [6] were used to calculate the corresponding E and T combinations that provide the lower bound. The results are also shown in Fig. 11 (blue solid circles).

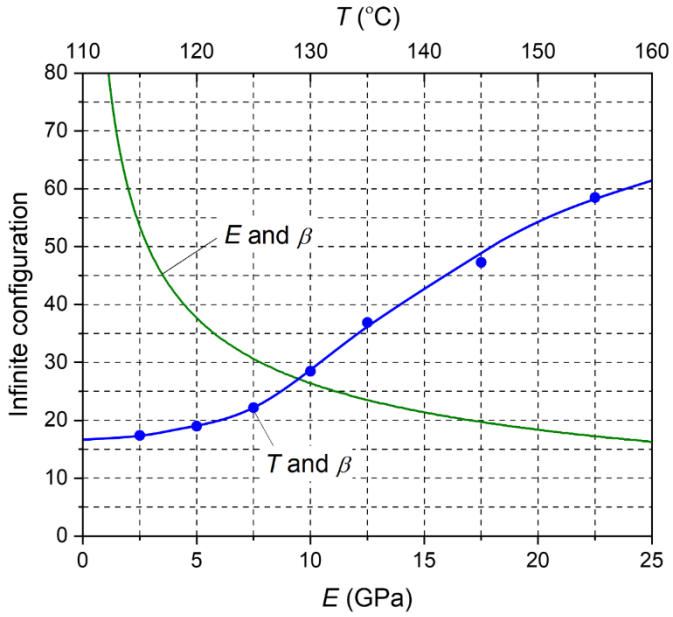

Fig. 11. E and β combinations required for the infinite configuration (green line); blue solid circles (E and T combinations) are obtained from temperature-dependent moduli [5].

For the upper bound of the configuration, a combined analysis of cure kinetics and heat generation should be conducted to estimate the extent of cure distribution within the specimen. Let's consider the well-known n^{th} order cure kinetics model, which is expressed as:

$$\frac{dp}{dt} = k_T(1-p)^n \tag{7}$$

where p and n are the extent of cure and the reaction order, respectively; k_T is a temperature-dependent rate constant, which can be defined by the Arrhenius

relationship. The governing equation based on the n^{th} order model that describes a temperature distribution during curing can be expressed as [10]:

$$\frac{K}{\rho}\left(\frac{\partial^2 T}{\partial r^2}+\frac{1}{r}\frac{\partial T}{\partial r}\right)+k_T(1-p)^n\Delta H=c_p\frac{\partial T}{\partial t} \tag{8}$$

where K, ρ, c_p and ΔH are the thermal conductivity, the density, the specific heat and the total exothermic heat, respectively.

The iterative numerical approach developed in Ref. [10] was utilized in this study. In the approach, the temperature distribution within a small-time step is calculated first through a transient thermal analysis, where a uniform heat generation caused by exothermic curing process is used as an input thermal loading. The resultant non-uniform temperature distribution is subsequently used to determine the extent of cure of the next time step using the cure kinetics model. The procedure is iterated until all part of specimen reaches the complete cure status (i.e., p = 1). The evolutions of temperature distribution and extent of cure obtained by recording the intermediate results during curing.

The analysis was conducted using the properties reported in Ref. [30] ($\Delta H = 18.0\,J/g; n = 0.93; k_T = 10^{-3}/s$). Representative distributions of temperature and extent of cure for β = 90 are illustrated in Fig. 12, where T = 130 °C and t = 478 second. The values of Δp_{max} (= $p_{in} - p_{out}$) at various temperatures were calculated as a function of β, where p_{in} and p_{out} are the values of cure extent at the center and the surface of a specimne, respectively. The results are shown in Fig. 13. It is to be noted that the green solid circle indicates the condition used for the results in Fig. 13. The horizontal line defines the acceptable criterion for Δp_{max} (= 1%) [10]. The

intersections points (red solid circles) indicate the largest configuration allowed at each temperature, which are plotted as a function of temperature in in Fig. 14 (solid red circles).

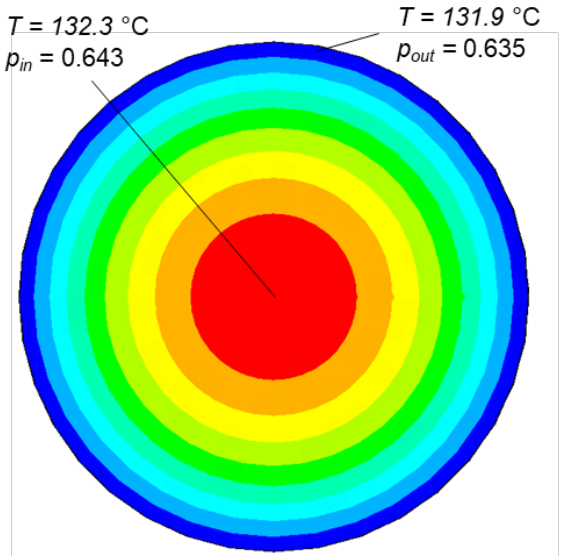

Fig. 12. Representative results for $\beta = 90$, obtained from the combined cure kinetics and heat generation analysis: the distributions of the temperature and extent of cure at $t = 478$ sec for $T_{cure} = 130$ °C [5].

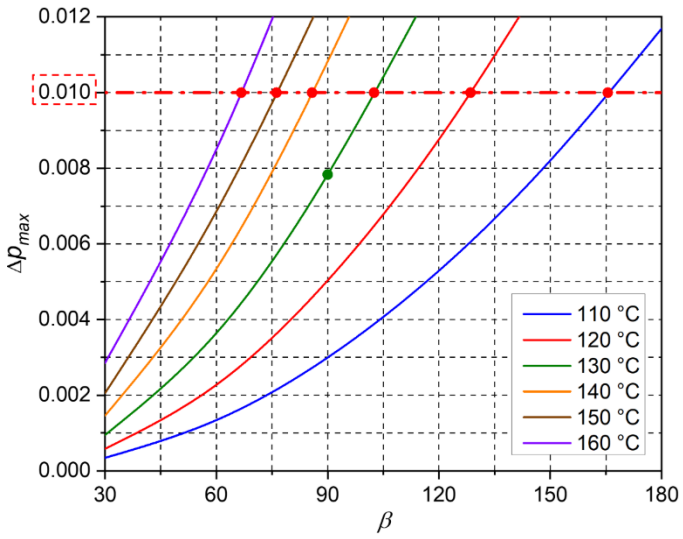

Fig. 13. Maximum difference of extent of cure as a function of configuration, where the horizontal line shows the criterion for Δp_{max} used in the study [5].

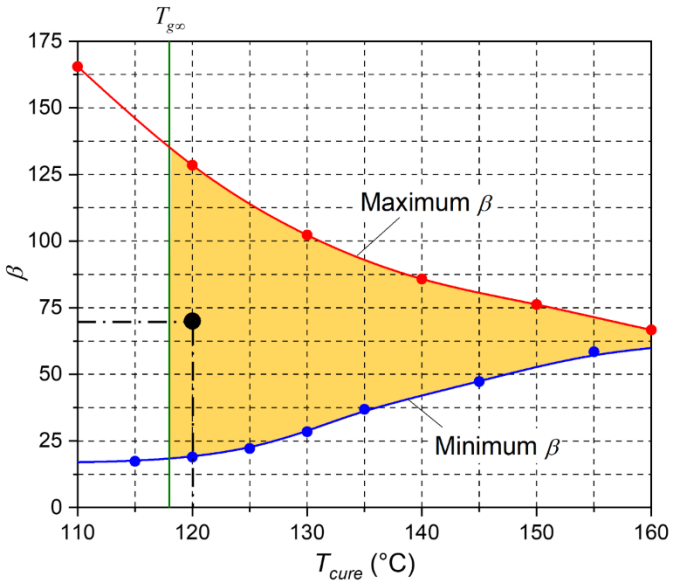

Fig. 14. Acceptable range for the proposed procedure (yellow shaded area), where the solid black circle indicates the values of configuration and T_{cure} used for the study: β = 70 and T_{cure} =120 °C [5].

The value of $T_{g\infty}$ is required to set the low bound of T_{cure}. It was measured by a dynamic mechanical analyzer (RSA3, TA Instruments). The value is shown as a vertical line (118 °C) in Fig. 14 together with the lower bound (blue solid dots in Fig. 14). The shaded area in Fig. 14 represents the acceptable range.

The value of β was chosen in the middle of the range considering the uncertainties of the properties used in the analyses. The value of T_{cure} was chosen at the lower side of the range to ensure that the specimen does not pass the gel point in Stage II. The solid black circle in Fig. 14 indicates the values of configuration and T_{cure} used for the study: β = 70 and T_{cure} =120 °C.

2.3.3 Testing and results

A procedure developed in Ref. [5] was used to fabricate an EMC specimen with an embedded FBG during Stage I. The experimental setup is shown schematically in Fig. 15. A metal mold is attached to a hot plate (HCP306S: Instec) for temperature control. An EMC pellet is placed inside the mold (diameter = 8.8 mm and length = 15 mm). The pressure regulator (ER3000: Tescom) provides air pressure to a pneumatic piston (121-DV: BIMBA). The piston force is transferred to a mechanical plunger that provides the required mold pressure (7 MPa), as shown in the inset. The maximum pressure of the compressed air line is only 0.69 MPa, but the required mechanical pressure is achieved by the pneumatic piston that has a diameter much larger than the plunger diameter. More details about the pressure application can be found in Ref. [6].

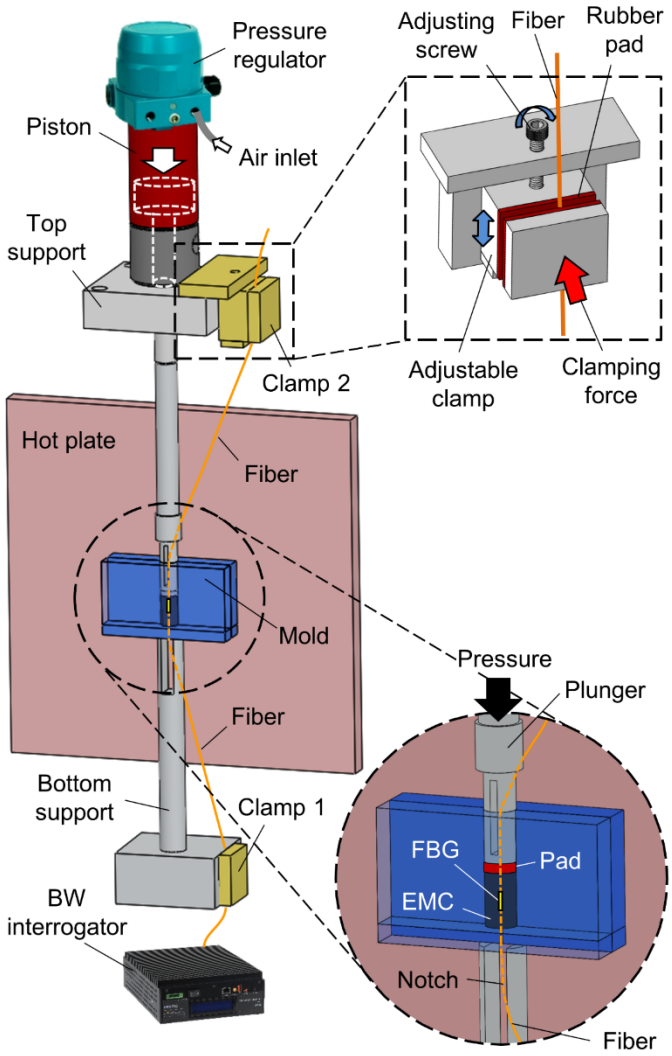

Fig. 15. Schematic diagram of the setup used for stage I, where the insets show the detailed view of the custom-designed mold and Clamp 2 [5].

The optical fiber (diameter = 125 μm) is inserted through a small through hole drilled in the center of the EMC pellet. As shown in the inset, the fiber position is adjusted in such a way that the Bragg grating (5 mm long) is located in the middle of pellet. The BW is documented by an FBG interrogator (si155: Micron Optics). To prevent leakage of EMC during pressure application, a silicone rubber pad is placed between the plunger head and the specimen. The mold is covered with an insulation box (not shown) before heating.

A pretension was applied to the fiber to make the fiber remain straight during Stage I. Two fiber clamps were used to apply a desired pretension. Clamp 1 was fixed to the bottom support, but the position of Clamp 2 was made adjustable using an adjusting screw to control the pretension amount, as illustrated in the second inset. A pretension of 3000 microstrain with an increment of approximately 100 microstrain was readily achieved.

Preliminary tests were conducted to determine the lowest T_{mold} while monitoring the plunger movement. The EMC pellet was collapsed without voids at 90 °C, and it was selected as T_{mold}. In Stage I, the pressure to the plunger was increased slowly to 0.5 MPa for the first 15 seconds, and it was quickly increased to 7 MPa for the next 5 seconds. The actual pressure applications used in Stage I are shown in Fig. 16.

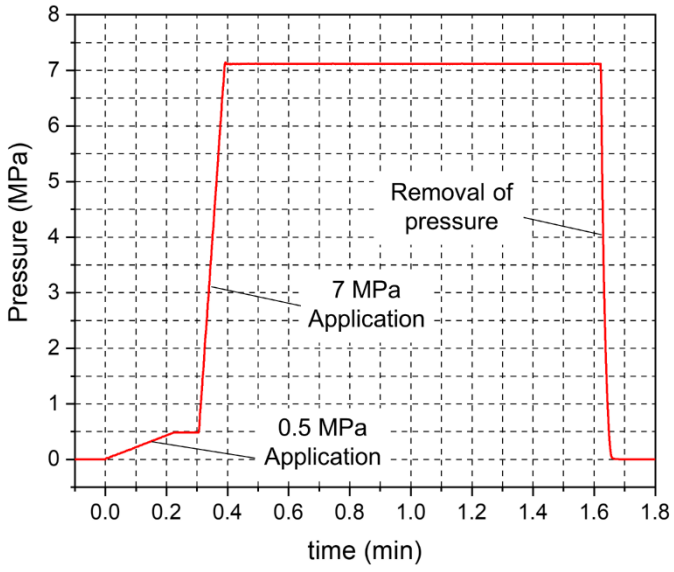

Fig. 16. History of pressure application in Stage I [5].

The setup was cooled down to room temperature slowly after the pressure was removed. The EMC specimen was separated from the mold. The molded specimen

after separation is shown in Fig. 17. The reflection spectra of the FBG before and after Stage I were measured to ensure the uniformity of the molded specimen. The results are also shown in Fig. 17. The spectra are nearly identical, which confirms that the specimen molded uniformly during Stage I.

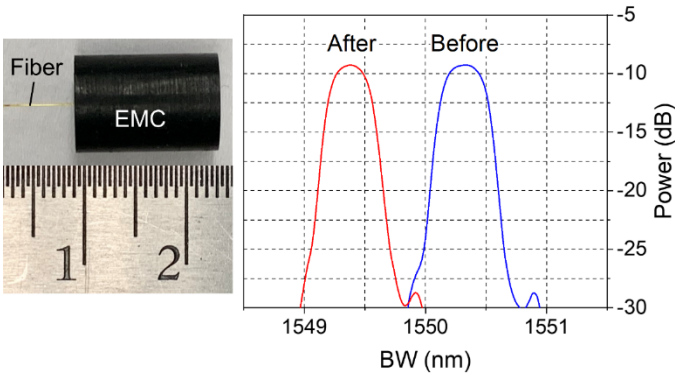

Fig. 17. Molded specimen obtained after Stage I and reflection spectra of FBG before and after Stage I [5].

The setup used for Stage II is shown schematically in Fig. 18(a). A metal fixture that had a hole slightly larger than the molded specimen was placed in a microprocessor-controlled convection oven (EC11A: Sun Electronic Systems). The convection oven was preheated to T_{cure} (120 °C). Then, the specimen was inserted in the preheated fixture through a small hole built on a sidewall of the oven. A silicone plug is used to block the hole while passing the fiber. This procedure minimized disturbance of the thermal equilibrium of the oven. The BW was recorded continuously during Stage II.

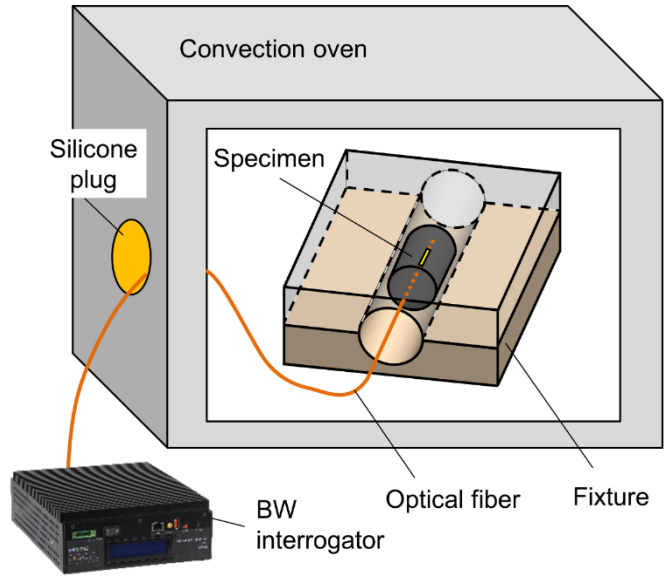

(a)

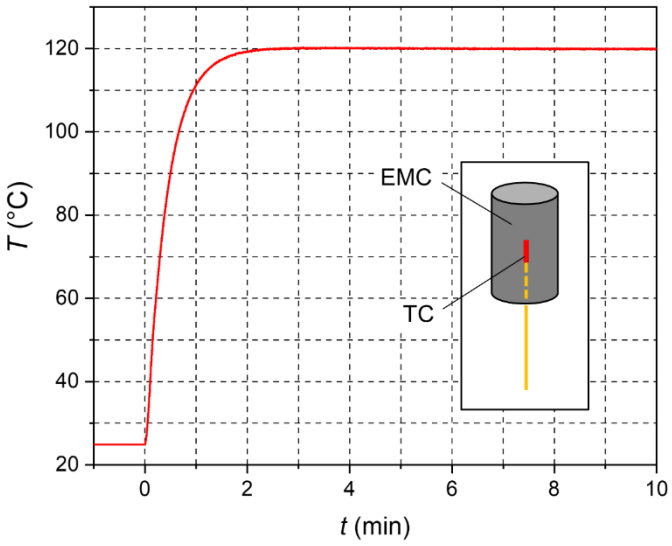

(b)

Fig. 18. (a) Schematic diagram of a setup for Stage II and (b) the temperature history of a specimen for the first 10 minutes of Stage II, where the x-axis represents elapsed time after the specimen is placed inside the fixture ($t = 0$) [5].

The performance of the setup was evaluated using an auxiliary specimen with a thermocouple embedded at the center. The temperature history of the thermocouple

specimen after placed inside the fixture (t = 0) to of Fig. 18(b). The temperature increased rapidly and became stable at T_{cure} within 3 minutes.

The complete BW history obtained during Stage II is shown in Fig. 19. The inset shows the BW during initial 40 minutes. As expected from the temperature data of Fig. 18(b), the BW increased rapidly during heating, and then became stable at T_{cure}. The BW remained constant for approximately 12 minutes (a plateau region), and began to decrease. The result confirms that the molded specimen did not pass the gel point of EMC before its temperature became stable at T_{cure}. The end of the plateau region was determined as the gel point.

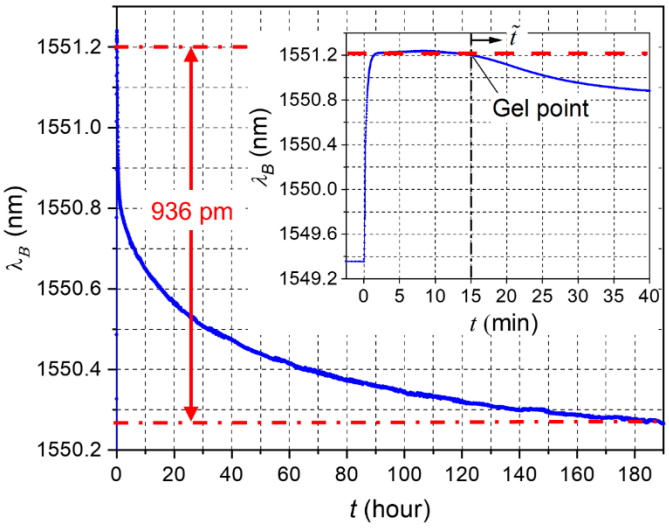

Fig. 19. BW obtained during Stage II where the inset shows the results of initial 40 minutes [5].

The total BW shift was determined from Fig. 19, and it was 936 pm. The total effective cure shrinkage, $\tilde{\varepsilon}_{\infty}$, was calculated from the BW shift using Eq. (3), and it was 0.077%. This is approximately 43% of the mold shrinkage value provided by the EMC manufacturer. The relationship between the effective cure shrinkage and the mold shrinkage can be found in Ref. [31].

2.3.4 Repeatability of the measurement

The measurement procedure implemented in the study was repeated to investigate its repeatability. The results obtained from the 2nd test during Stage II are compared with the original test results (Fig. 19) in Fig. 20, where the Bragg wavelength changes ($\Delta\lambda_B$) after the gel point were calculated for direct comparison. It is clear from the comparison that the time-dependent histories of Bragg wavelength (λ_B) are virtually identical. The total Bragg wavelength changes of the two tests are 936 and 916 pm, which correspond to the ECS values of 0.077% and 0.075%, respectively. In spite of the complexity involved in the testing procedure, including the high-pressure application, the ECS values obtained from two completely independent measurements differ only by 2%. The gel point detected from both tests were also very close (≈ 15 minutes), which was another indication that the measurement procedure was repeatable.

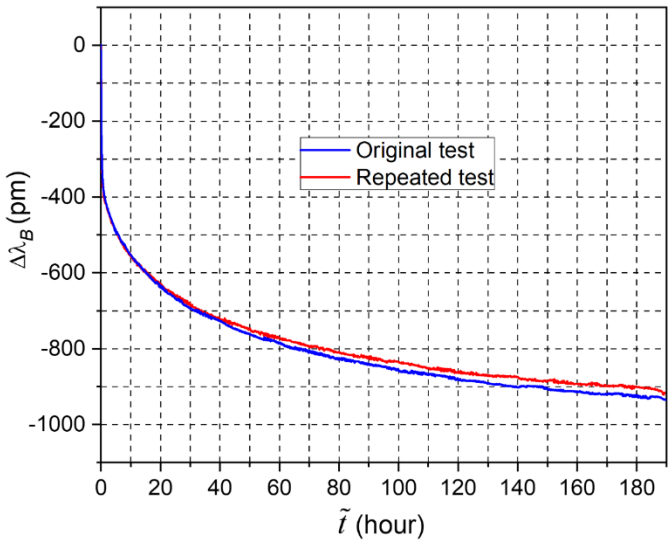

Fig. 20. BW changes obtained from the original test are compared with the repeated test [5].

2.3.5 Residual stress prediction in transfer molding

During the transfer molding processes described in Fig. 2, the molding compound cures rapidly at the mold temperature, and quickly passes its gel point (typically within a couple of minutes). As mentioned earlier, the molding compound becomes a deformable solid at the gel point. After the gel point, the pressure to fill the cavities is no longer transferred to the molding compound inside the cavities, although the pressure is maintained; i.e., the mold pressure deforms only the molding compound near the transfer pot (yellow area). This is illustrated schematically in Fig. 21. This provides the technical rationale for the reason why the effective cure shrinkage must be measured after the mold pressure is removed for the prediction of residual stresses produced by the transfer molding process.

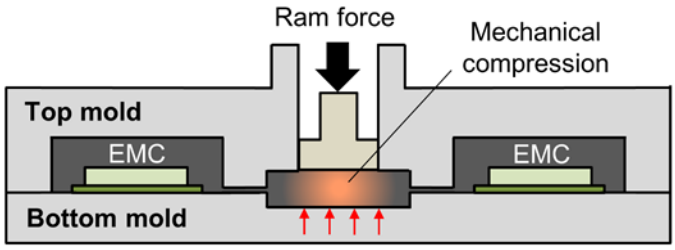

Fig. 21. Schematic illustration of stresses on EMC immediately after EMC passes its gel point [5].

Chapter 3: Measurement of Warpage During Molding Processes

3.1. Technical background

3.1.1 Warpage measurement of packages

The warpage of plastically encapsulated packages is critical, and extensive numerical modeling has been conducted to predict the warpage. The warpage has been measured to verify the validity of numerical models used for warpage prediction. The warpage is generated due to the temperature change as well as the molding process. The measurement of the warpage is typically done in an open environment after the sample is removed from the mold. To measure the warpage generated only by the molding process, however, the warpage should be measured during the molding process.

Noncontact warpage measurement techniques have been widely used [32]. Most of the commonly used measurement techniques are full-field measurement techniques, which measure the warpage of the entire surface of the sample. A couple of frequently used full-field measurement techniques and a point measurement technique are reviewed.

3.1.2 Full-field measurement technique

Shadow moiré is the most widely used full-field, out-of-plane displacement measurement technique in the various fields of solid mechanics [33]. This method requires a reference grating, a light source, and a camera, and the setup is illustrated in

Fig. 22. The surface of the specimen should be matte, and it can be achieved by spraying a matte white paint on the surface. A linear reference grating is placed very close to the specimen surface.

The out-of-plane displacement of that point in the surface is linearly proportional to the fringe order at that point [34, 35]. The shadow moiré is easy to implement. The surface of the specimen should be diffusive, and the surface treatment is usually required before the measurement. Additionally, there should be enough open area near the incident and reflected light during the measurement.

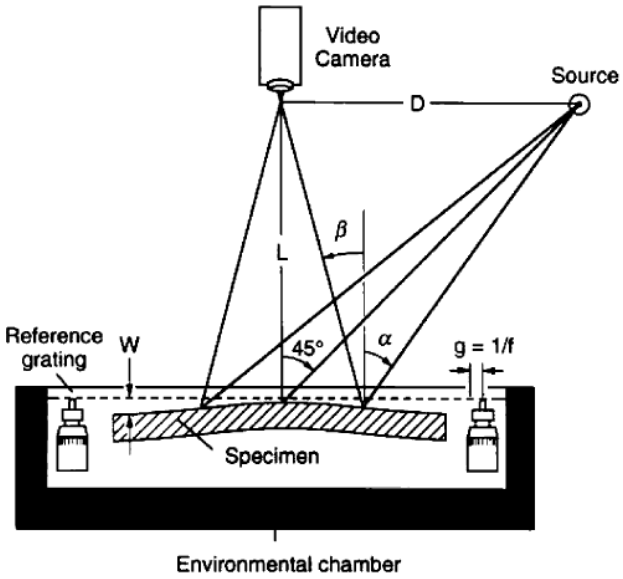

Fig. 22. Schematic illustration of the shadow moiré setup [33].

Digital image correlation (DIC) is a full-field, 2D or 3D deformation measurement technique [32, 36]. The method tracks the changes of small distinct features within the subset of the image, and the correlation is calculated to determine the movement. There are many correlation calculation methods are available, and the

sum of the squared differences (SSD) correlation criterion is a commonly used method, and the equation for 2D case is defined as [45, 46]:

$$C_{SSD} = \sum_{i=-M}^{M} \sum_{j=-M}^{M} \left[f(x_i, y_i) - g\left(x_i', y_j'\right) \right]^2 \tag{9}$$

where x_i, y_i are coordinates of a point before movement, x_i', y_i' are coordinates of the point after movement, and $f()$ and $g()$ are the brightness distribution function of images.

The warpage of the sample can be measured by using the 3D DIC, which is illustrated in Fig. 23(a). A speckle pattern with good contrast is added to the specimen surface before the measurement, and the position of the patterns is recorded by two cameras during the measurements. Then, the position of each point is determined by using the stereo triangulation principle [37].

The DIC does not require a reference grating, and it can measure samples in various sizes. However, the speckle pattern should be applied to the sample before the measurement. The measurement is sensitive to the mechanical vibration because small changes in the camera positions can cause large measurement inaccuracy [38, 39]. Like the shadow moiré case, there should be enough open space for two cameras to monitor the entire specimen.

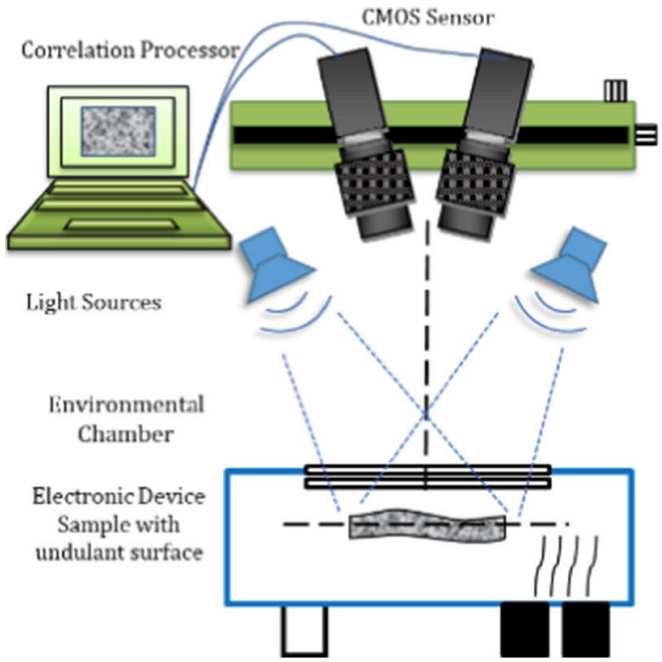

Fig. 23. Schematic illustration of DIC experiment system [36].

In the full-field measurement technique, the entire surface of the specimen is measured, and the whole specimen should be exposed to the open environment. In addition, the surface preparation is required for many measurement methods before testing.

3.1.3 Point measurement technique

A point measurement technique has been used to measure the out-of-plane displacement of a point or local area of the specimen. The point measurement uses laser beams with a small diameter that illuminates the specimen surface, and the reflected beams from the surface of the specimen are measured by a camera or sensor. The slope of the specimen is measured based on the angle change of each reflected beam, and the curvature or deflection can be calculated.

The surface curvature was measured by using multiple laser beams during the temperature changes in Ref. [40]. The changes of the reflected light due to the deformation of the sample is illustrated in Fig. 24, where a 1-D curvature is considered. When the distance between the adjacent laser beam is made small, the curvature can be calculated by

$$\frac{d^2y}{dx} \approx \frac{\left.\frac{dy}{dx}\right|_{x_2} - \left.\frac{dy}{dx}\right|_{x_1}}{x_2 - x_1} \tag{10}$$

where $y(x)$ is a function of the curve, and x_1 and x_2 are two closely located points.

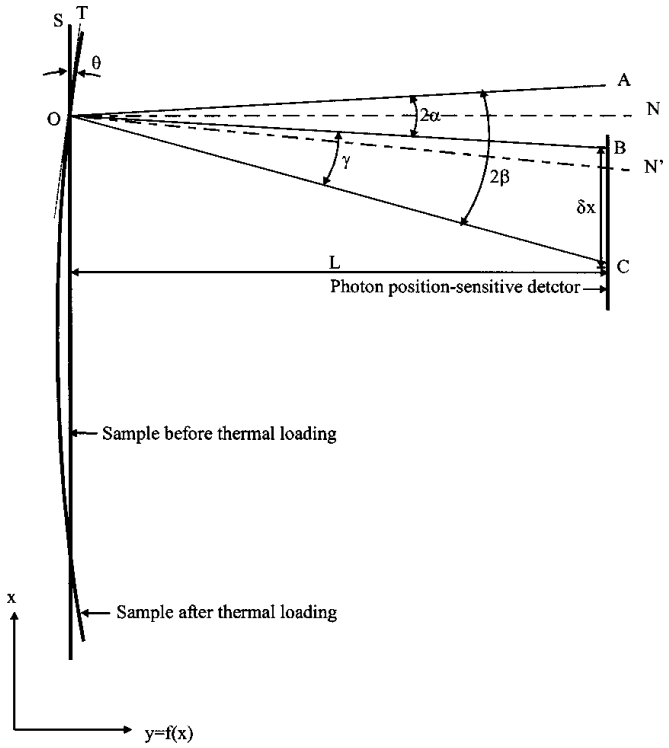

Fig. 24. Incident and reflected beams before and after bending of the sample [40].

For the 2-D case, four laser beams originated from one beam are employed. In the study reported in Ref. [40], a He-Ne laser was used as a light source, and multiple beams are generated by using beam splitters and mirrors. The experimental setup is

shown in Fig. 25. Three of them were used to calculate the 2-D surface curvature along two perpendicular directions.

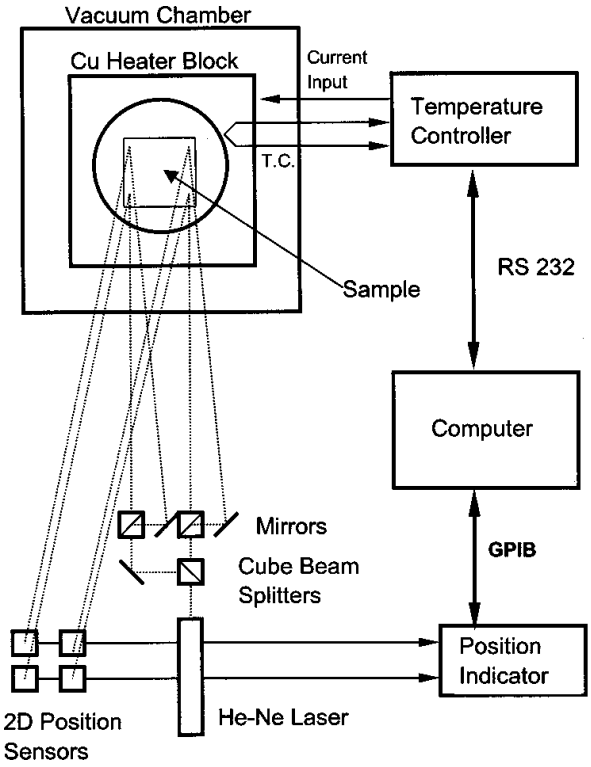

Fig. 25. Experimental setup for 2D surface curvature measurement used in Ref. [40].

The curvature of a flip-chip-on board package was measured in Ref. [72]. A die surface was polished to reflect laser beams, and the incident angles of the laser beams were less than 2°. 2-D photo detectors and position indicators were used to measure the position of the beams. The curvatures along two perpendicular directions were measured in the while heating from 25 to 170 °C.

An *in situ* measurement of the curvature beams during a film deposition is done by using an array of laser in Ref. [41]. The measurement setup is illustrated schematically in Fig. 26. During the measurement, the change of the mean differential

spacing, δd, was monitored, and the curvature was calculated using the following equation:

$$\frac{1}{\rho} = -\frac{cos\alpha}{2L}\frac{\delta d}{D_0} \tag{11}$$

where ρ is the curvature, α is the incident angle, L is the optical path length of the laser beams, and D_0 is the initial value of the mean differential spacing. For a thin coating, the stress thickness product ($\sigma \cdot \tau$) was proportional to δd so that this method was used to monitor the stress along a growing film.

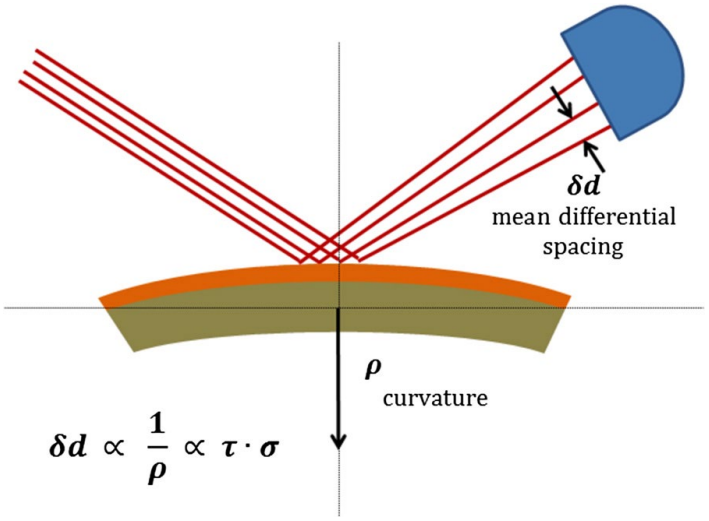

Fig. 26. Schematic representation of the curvature measurement method [41].

A square 3 × 3 array of laser beams were directed to the center of the substrate. The surface of the substrate was polished for the beam reflection. The distance between the beams was 1 mm, and the incident angle was 30°. The curvature was measured during the film deposition process based on the movement of the beams.

The point measurement does not require a special preparation of the sample before the measurement if the surface is smooth enough for the light beam to be reflected. This makes the in-line warpage measurement possible during the process.

Since the point measurement method measures the out-of-plane displacement of local area of the specimen, a larger measurement area with multiple beams could provide more accurate measurement.

3.2. Proposed technique for in-line warpage measurement

The molding process of the EMC requires a metal mold, and the EMC is surrounded by the mold since a large amount of pressure is applied to the EMC. The full-field out-of-plane displacement measurement techniques cannot be used for the measurement during the molding process because (1) the entire specimen cannot be exposed due to the mold, and (2) the specimen surface preparation for the measurement cannot be done.

The point measurement can be utilized for the molding application since it measures a local area of the specimen, but the existing techniques are not ideally suited to warpage measurement during the mold process because only a small area of the specimen is measured by using 2 or 3 beams along a line, i.e., not applicable to the warpage of the larger area of the specimen. Other practical limitations of the existing techniques include that (1) the optical setup is too complicated to be used the molding process and to be sensitive to environmental disturbances such as vibrations and (2) the multiple beam tracking is difficult to achieve using a single imaging system.

To cope with the above difficulties, a novel in-line warpage measurement technique is proposed and implemented in this thesis. The technique is essentially based on the point-based measurement principle. Two novel improvements are made to advance the technique for in-line warpage measurement with required accuracy.

The proposed technique is illustrated schematically in Fig. 27 where the side view and the top view are shown in (a) and (b), respectively. A single mode laser diode (LD) produces extremely stable multiple beams, and the intensity of each beam can be controlled by a power supply that provides a required current to the LD. The beams are reflected from the specimen surface and are impinged on an optical target that is subsequently viewed by a high resolution CCD camera. How the beams are sent to the specimen surface without being blocked by the metal mold structure is illustrated in (b). The beam movements caused by warpage are calculated by a unique imaging processing routine.

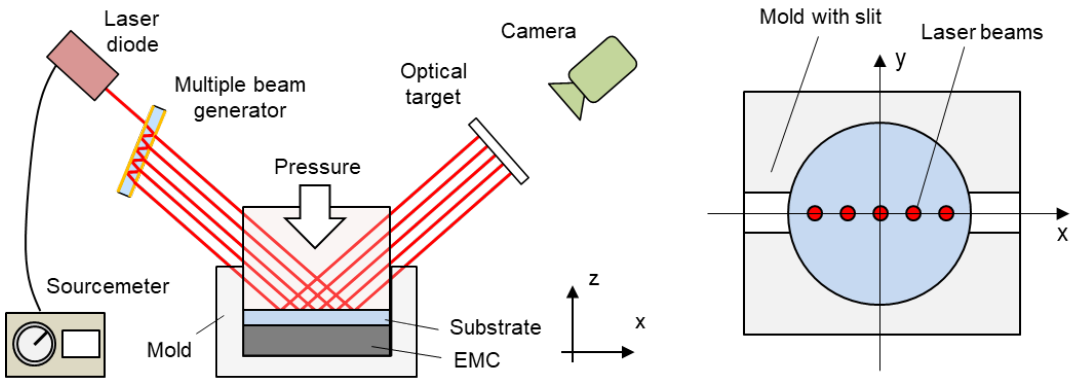

(a) (b)

Fig. 27. Schematic diagram of parts in the warpage measurement system in (a) side view, (b) top view.

In this chapter, the governing equation that defines a relationship between the beam movements and the warpage is described first. Then, the two improvements are described in detail, namely (1) Fabry-Perot based multiple-beam generation in

conjunction with current-dependent laser diode power and (2) binarization-based beam tracking procedure.

3.2.1 Calculation of movement and governing equation

The warpage causes beam movements. The movement of the beam generated by the warpage is illustrated in Fig. 28, where a total of five beams are used for illustration. The beams are evenly distributed to the centerline of the specimen surface. The distance from the center is 0, $1/3a$, $2/3a$ for beam 0, ±1, and ±2, respectively, where a is the radius of the specimen.

Under the ideal situation, the slope at the center ($r = 0$) does not change even when warpage occurs. Therefore, the beam at the center (0^{th} beam) should not have any movement during the test. The other four beams will move, and the following derivations are made to provide the relationship between the movements and the slope.

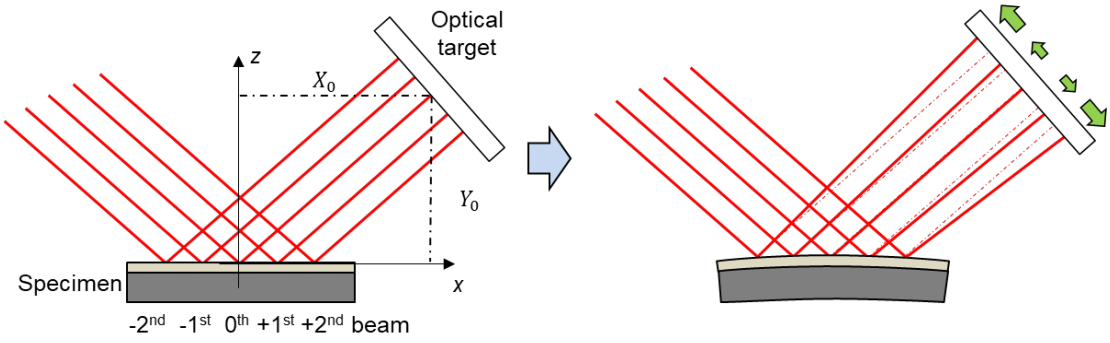

(a) (b)

Fig. 28. Schematic illustration of the incident and reflected laser beams projected to the optical table (a) before, (b) after the warpage is generated.

The calculation of the slope is based on the movement of the beam on the optical target. The position of the reflected beam on the optical target is calculated by finding the intersection between two linear functions describing (1) reflected beam, (2) surface of the optical target. The movement of the beam illuminating a point r away from the middle of the specimen is described in Fig. 29. Linear equations required for the calculation can be defined as:

$$z = \tan(\theta) \cdot (x - r) \quad \text{for reflected beam before angle change}$$
$$z = \tan(\theta - 2\alpha(r)) \cdot (x - r) \quad \text{for reflected beam after angle change} \qquad (12)$$
$$z = -\tan\theta((x - X_0) + Y_0 = -tan\theta \cdot x + 2Y_0 \quad \text{for optical target}$$

where θ is the angle between incident beam and *x*-axis, *r* is the distance of the point of the specimen from the center, (X_0, Y_0) is the position of the reflected 0th beam projected to the optical target. This point is used because the 0th beam does not move due to the warpage. Since $Y_0 = tan\theta \cdot X_0$, the equation for the optical target can be expressed as $y = -tan\theta \cdot x + 2Y_0$.

r ranges from -*a* to +*a*, and the slope $\alpha(r)$ generates the movement of the beam on the optical target by $d(r)$. The location of the beam projected to the optical target before and after the movement of the beam is $(X(r), Y(r))$ and $\left(X'(r), Y'(r)\right)$, respectively. The amount of the *z* displacement generated by the warpage is $\Delta w(r)$. The beam movement generated by $\Delta w(r)$ is ignored since it is negligibly small. More details related to this will be discussed later.

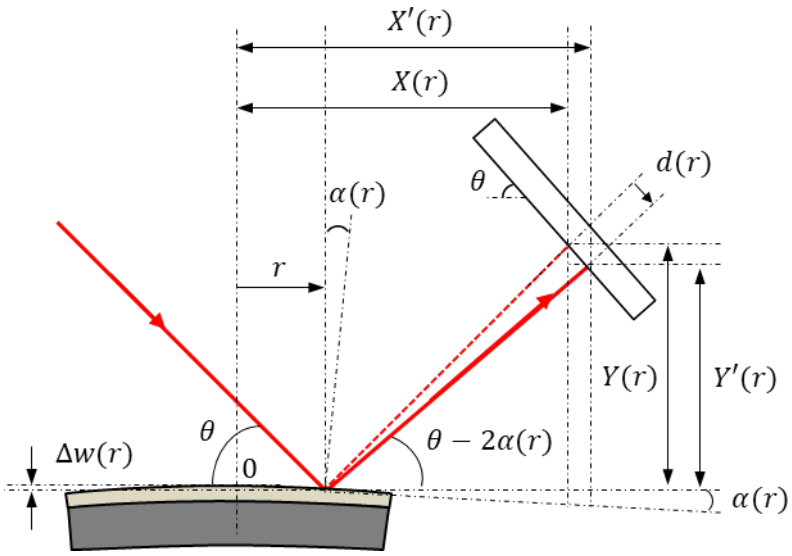

Fig. 29. The illustration of the movement of the i^{th} beam at the distance r from the center due to the warpage.

The location before and after the movement can be expressed as:

$$\begin{aligned} X(r) &= \frac{\tan\theta \cdot r + 2Y_0}{2tan\theta} \\ Y(r) &= -tan\theta \cdot X(r) + 2Y_0 \\ X'(r) &= \frac{\tan\big(\theta - 2\alpha(r)\big) \cdot r + 2Y_0}{\tan\big(\theta - 2\alpha(r)\big) + tan\theta} \\ Y'(r) &= -tan\theta \cdot X'(r) + 2Y_0 \end{aligned} \tag{13}$$

where θ is the incident angle of the beam, X_0 and Y_0 are the horizontal and vertical location of the 0[th] beam on the optical target. Then, the movement of the beam $d(r)$ can be calculated as:

$$\begin{aligned} d^2(r) &= (X'(r) - X(r))^2 + (Y'(r) - Y(r))^2 \\ &= (1 + \tan^2\theta)(X'(r) - X(r))^2 \\ d(r) &= \sqrt{1 + \tan^2\theta}\,(X'(r) - X(r)) \end{aligned} \tag{14}$$

It should be noted that $d(r)$ becomes negative when r is negative. The slope change can be calculated from the beam movement by:

$$X'(r) = \frac{\tan\left(\theta - 2\alpha(r)\right) \cdot r + 2Y_0}{\tan\left(\theta - 2\alpha(r)\right) + tan\theta} = X(r) + \frac{d(r)}{\sqrt{1 + \tan^2\theta}} \tag{15}$$

$$\alpha(r) = \frac{1}{2}\left[\theta - \tan^{-1}\left\{\frac{-2Y_0 + tan\theta\left(X(r) + \frac{d(r)}{\sqrt{1 + \tan^2\theta}}\right)}{r - X(r) - \frac{d(r)}{\sqrt{1 + \tan^2\theta}}}\right\}\right] \tag{16}$$

When the warpage of the bimaterial specimen is generated, the slope is symmetric, and the slope changes linearly as a function of r, except near the end of the specimen. Since the 5 beams cover up to 2/3 of the diameter, the slope changes linearly within that range. Based on the calculated slope, the curvature is calculated by:

$$\kappa = \frac{\partial\alpha(r)}{\partial r} \tag{17}$$

where κ is the curvature. A linear regression of the slope is done to determine the curvature for each time step, and the illustration of the beam movement, slope as a function of r, and the curvature determination in Fig. 30.

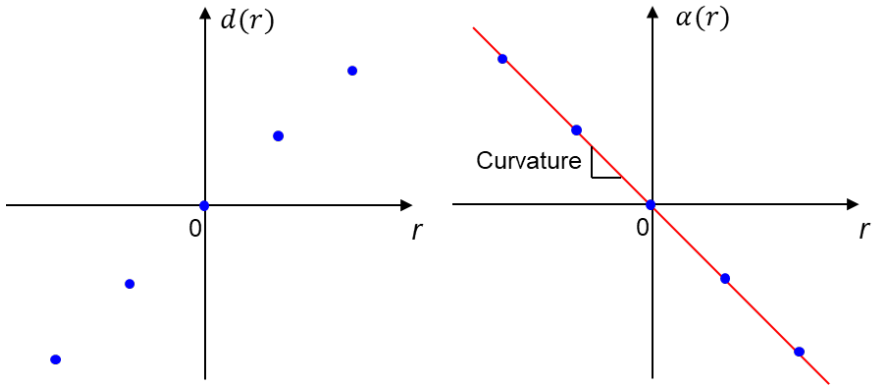

(a) (b)

Fig. 30. The illustration of (a) the beam movement as a function of r, (b) the slope and the linear fitting for determining the curvature.

Finally, the warpage of the specimen is calculated from the fitted curvature:

$$\Delta w(r) = \frac{\kappa \cdot r^2}{2} \tag{18}$$

3.2.2 Fabry-Perot based multiple-beam generation

The proposed in-line warpage measurement is based on the movements of multiple laser beams that are directly reflected from the specimen surface along a line. Beam splitters can be used to generate multiple beams (see Fig. 25). An additional beam splitter is required to produce one additional beam (e.g., three beam splitters are required to produce four beams). Besides practical considerations associated with the size of commercially available beam splitters, beam splitters should be aligned accurately, and their positions are securely fastened to send and maintain multiple beams on the pre-defined positions of the specimen surface.

To cope with the above problem, this study utilizes the concept of Fabry-Perot interferometer [43] to produce multiple beams. As illustrated in Fig. 31, both sides of an optical glass are coated with a partially reflective layer. Multiple reflections are generated inside the glass, and each reflection produces an additional beam. Since the two surfaces of the glass are parallel, the angle of each reflected beam is identical. No tuning is necessary, and the locations of multiple beams are extremely stable.

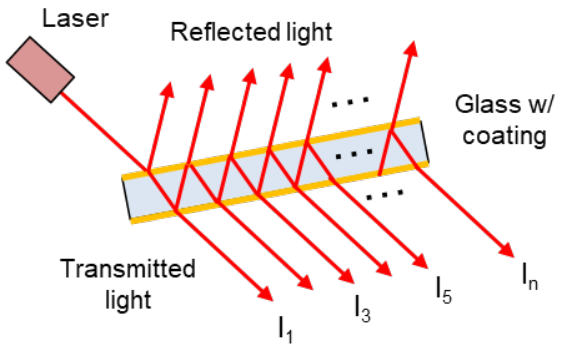

Fig. 31. Multiple beam generation by using the concept of Fabry-Perot interferometer.

Assuming light absorption though the coating is negligible, the intensity of the i^{th} transmitted beam can be depressed as

$$I_i = TR^{2(i-1)}T \quad \text{for } i \text{ from 1 to n} \tag{19}$$

where T and R are the transmittance and the reflectance of the coating, respectively. The intensities of the transmitted beams are shown as a function of reflectance in Fig. 32(a). The intensity of the beams normalized by the intensity of the first beam is shown in Fig. 32(b). Due to multiple reflections, transmitted beams do not have the constant intensity. When the reflectance is small, the intensity of the first beam is very high due to the high transmittance, but the intensity gets small quickly for the higher order of the beams due to their small reflectance. In opposite, the intensity of the first beam is small when the reflectance is high, but the intensity of the higher order beams gets closer to the first beam intensity, as clearly shown in Fig. 32(b). Therefore, the metallic coating with a high reflectance is more suitable for the multiple beam measurement, but the intensity of the higher order of beams will be still smaller than the intensity of the first beam unless the reflectance is almost 1.

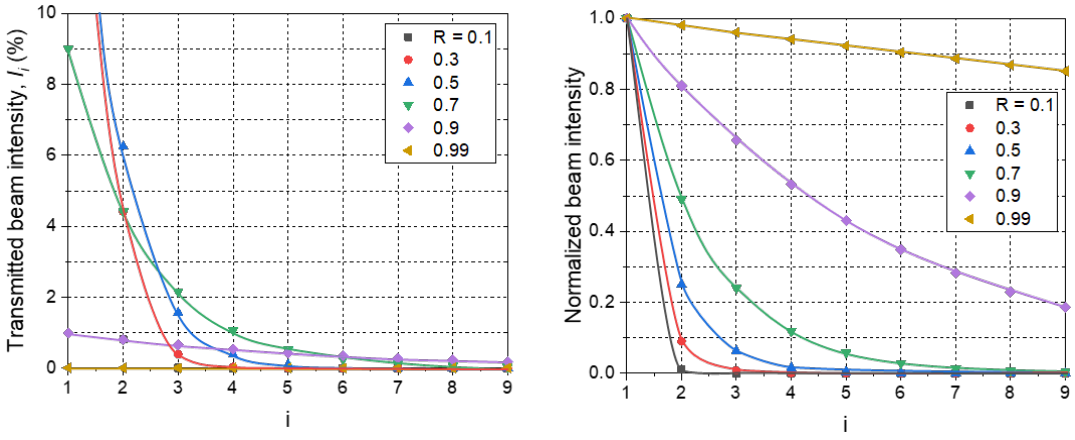

(a) (b)

Fig. 32. Theoretical calculation of (a) the transmitted beam intensity, (b) normalized intensity of the transmitted beams.

The inherent intensity variations of multiple beams produced by the current method can be readily normalized by using the input current-dependent power output of a laser diode. A typical output power of a laser diode as a function of input current is sown in Fig. 33. The output power is linearly proportional to the input current after a threshold value of current. This can be used effectively to make each beam intensity nearly identical like shown in Fig. 34, which is critically required for the proposed image processing scheme. To utilize the glass with the high reflectance coating, the maximum power of the laser diode should be large enough to make the intensity of the beams large enough to be captured.

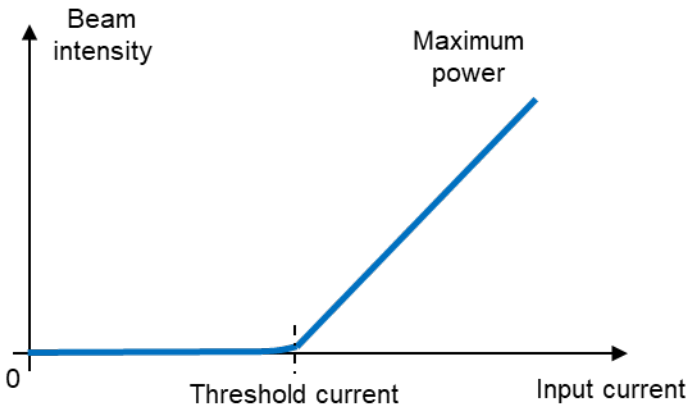

Fig. 33. Schematic illustration of laser diode beam intensity as a function of input current.

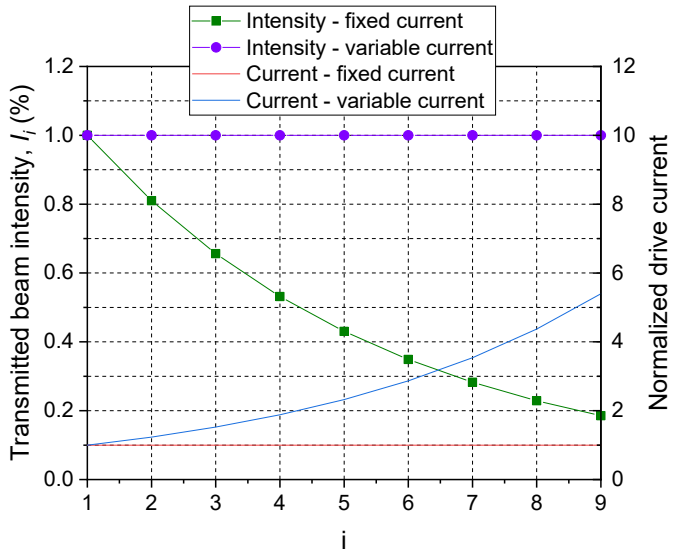

Fig. 34. The beam intensity of transmitted beams when the input current is constant and variable to make the intensity of the beams the same.

3.2.3 Simultaneous detection of multiple beam movement

In the image captured by the camera, each pixel has its own light intensity. The number of pixels covered by the laser beam depends on the size of the beams, and it

could be as small as a pixel, as illustrated in Fig. 35(a), or more practically, the size of the beam is larger than the pixel size, as illustrated in Fig. 35(b). Each grid cell in Fig. 35 represents a pixel of a digital camera sensor.

The identification of the position of the beam is relatively easy in Fig. 35(a) since only a single pixel is illuminated. In real applications, the size of the pixel is as small as a few micrometers, and the laser beam covers multiple pixels, as shown in Fig. 35(b). After the beam is moved, as shown in Fig. 35(c), the intensity profile of the beam shifts, as shown in Fig. 35(d). Thus, the pixel intensity gradually changes, and the accurate tracking of the beam movement becomes challenging. The sub-pixel calculation capability is typically required for accurate beam tracking.

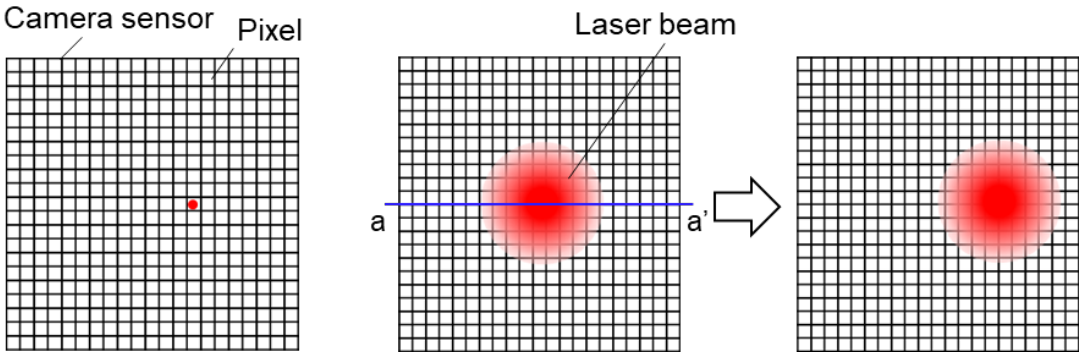

(a) (b) (c)

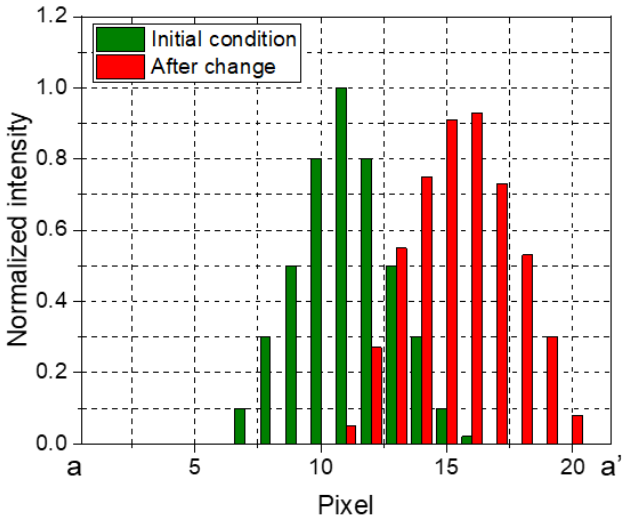

(d)

Fig. 35. Illustration of (a) an idealized laser beam with the size of a pixel, (b) an actual laser beam with the size of multiple pixels projected onto a camera sensor, (c) the actual laser beam after the movement, and (d) the intensity profile of the beam along the line a-a' before and after the movement.

3.2.3.1 Problem with the DIC Method

The 2D DIC method was first considered to track the movement of the multiple beams on the diffusive surface. For the tracking of each beam, a subset of the image can be defined, like shown in Fig. 36, and the tracking of the movement by using the 2D DIC is illustrated. In the multiple beam case, the subset for each beam needs to be defined separately. As presented earlier, the DIC method is based on the correlation of small features, those random pattern of the image should be retained after the change for good tracking results. If the intensity profile within the beam is randomly changed by illuminating other parts of the diffusive surface after the movement, it gets hard to achieve a good correlation between two images.

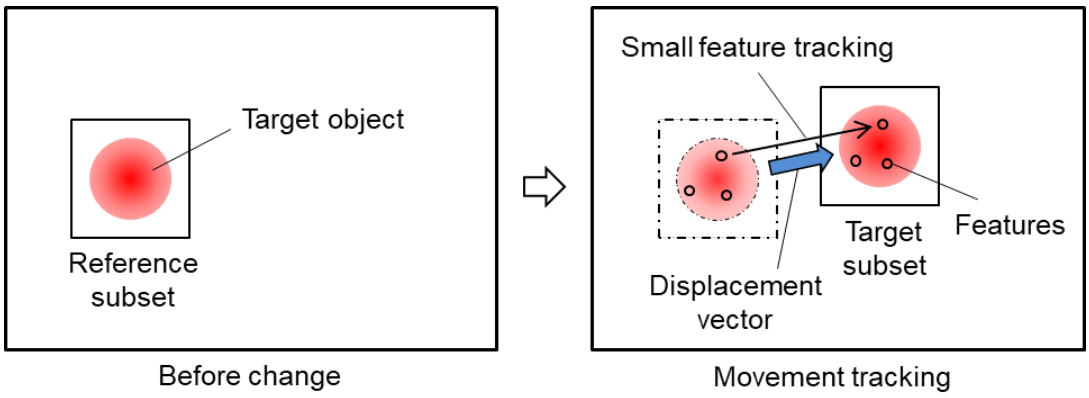

Fig. 36. Illustration of the beam movement tracking with 2D DIC.

During the measurement, the reflected laser beam from the specimen surface is captured by the camera. Due to the small size of the image sensor, the reflected beams are projected to a diffusive optical target, and the camera with a lens captures the image of the optical target. Ground glass is a transmissive diffuser, and the surface of a glass is made rough by using a method like sandblasting. There is an inherent randomness of the surface, and the beam intensity profile could be changed after passing the ground glass like illustrated in Fig. 37. Also, the intensity profile could change when the beam is illuminated to the other locations of the ground glass. The change of the intensity distribution by illuminating other parts of the ground glass is called the location effect, and this location effect could cause an error of the beam tracking.

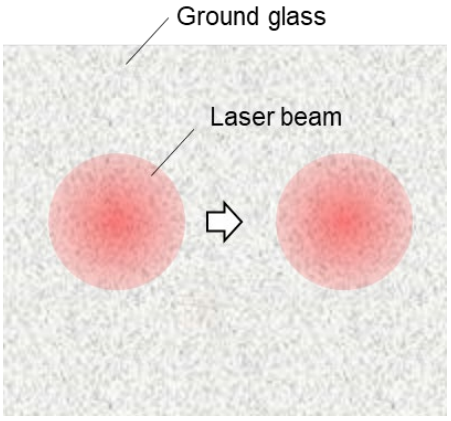

Fig. 37. Illustration of the intensity pattern change of the beam due to the ground glass location effect.

As an example, the collimated laser diode beam after passing the ground glass is shown in Fig. 38(a), and the intensity profile is shown in Fig. 38(b-d). The intensity distribution of the beam changes after passing the ground glass. The intensity distributions for two ground glass locations are shown in Fig. 38(b-d), and it clearly shows the change of the intensity distribution. Even after the intensity distribution changes, the DIC can determine the 0 movement if the beam does not move. However, the randomness of the region at the different location of the ground glass alters the intensity profile of the beam even though the beam does not move. The location effect of the ground glass can be checked by moving only the ground glass while keeping the laser and the camera stationary. The ground glass is moved 0.5 mm in each trial, and this was repeated 5 times. Since the camera and laser do not move, the amount of the movement is ideally 0, and the movement of the beam detected by the image processing methods indicates the ground glass location effect.

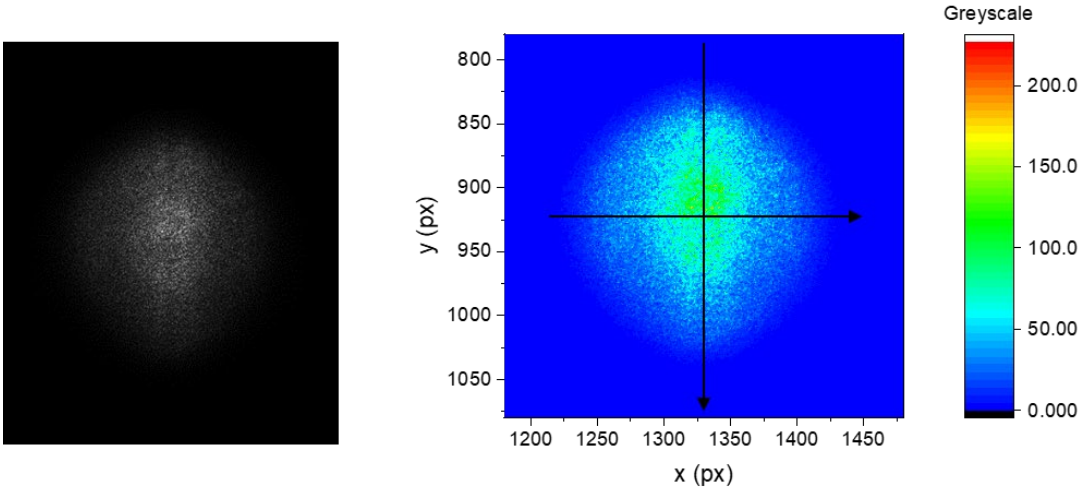

(a) (b)

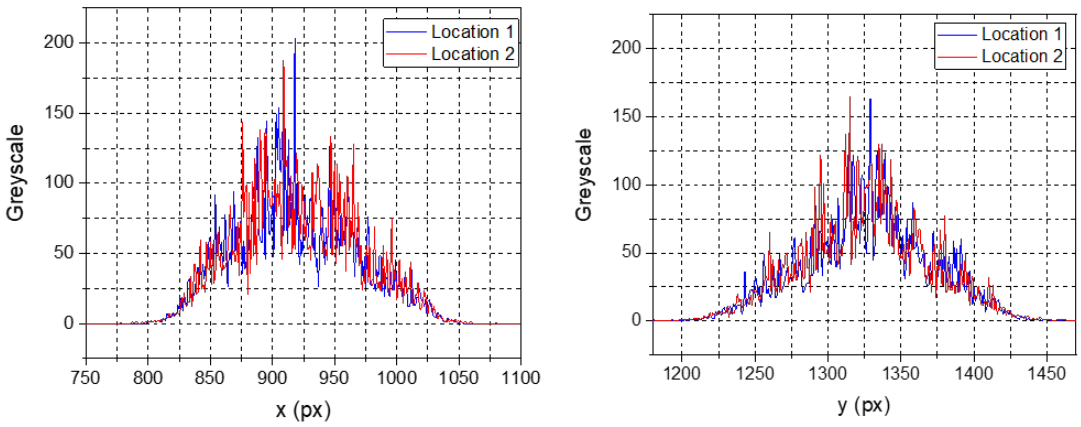

(d) (e)

Fig. 38. (a) beam after passing the ground glass captured by the camera, (b) intensity profile of the beam, (c) intensity through the horizontal line at the center, (d) intensity through the vertical line at the center of the beam for two cases.

The movement of the beam tracked by the 2D DIC is shown in Fig. 39. The amount of the movement shows the ground glass location effect, and it is up to 1.75 px. When the ground glass is moved, the light intensity pattern of the beam randomly

changes, and it makes the DIC technique difficult to get the good correlation between the images before and after the movement.

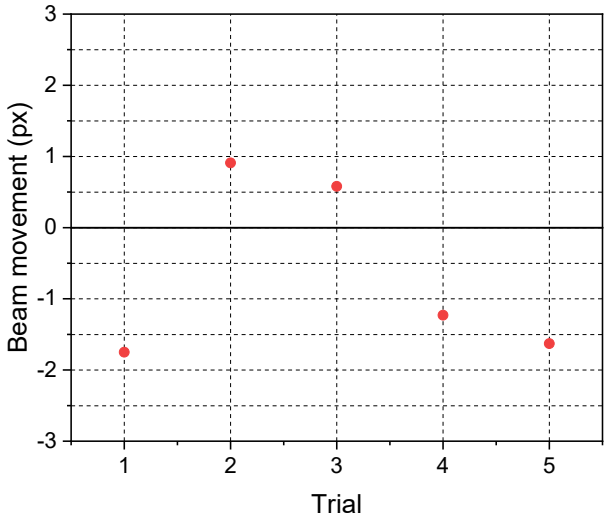

Fig. 39. The beam tracking results of the 2D DIC method; the amount of the movement indicates the error generated by the location effect.

3.2.3.2 Proposed binarization-based tracking method

The tracking of the target objects also can be done based on the movement of the center of the object without considering the intensity profile of the pixel within the object. Unlike the DIC method, the correlation of the small features within the object do not have to be tracked, and the tracking could provide a better result if the light intensity pattern randomly changes due to the movement. The movement tracking of the binarized image is illustrated in Fig. 40. A binarization process simplifies the light intensity distribution of the object by binarizing the pixel intensity based on the threshold:

$$I'(x_i, y_i) = 1 \text{ for } I(x_i, y_i) \geq T$$
$$I'(x_i, y_i) = 0 \text{ for } I(x_i, y_i) < T \tag{20}$$

where I and I' is the pixel intensity of the pixel at the point x_i, y_i before and after the binarization, and T is a threshold for binarization. The binarization method eliminates the effect of intensity variations except for the intensity near the threshold. When there are pixel intensity variations like shown in Fig. 38(d, e), the shape of the object could become very rough, and the tracking of the movement could become noisy. To minimize this effect, the smoothing of the pixel intensity can be done by using a method such as Gaussian smoothing [47]:

$$G(x, y) = \frac{1}{2\pi\sigma^2} e^{-\frac{x^2+y^2}{2\sigma^2}} \tag{21}$$

where x, y are horizontal and vertical distance from the origin, σ is the standard deviation of the Gaussian distribution.

In the binarized image, there might be multiple objects detected, and the target object needs be identified among them. For example, the objects can be sorted by the size, and the target object can be found. The centroid of the object can be calculated as following and be used to calculate the movement of the object:

$$\bar{x} = \frac{\sum_{i=1}^{n} x_i}{n}$$
$$\bar{y} = \frac{\sum_{i=1}^{n} y_i}{n} \tag{22}$$

where $\bar{x}$, $\bar{y}$ is the centroid of the object, n is the number of pixels of the object.

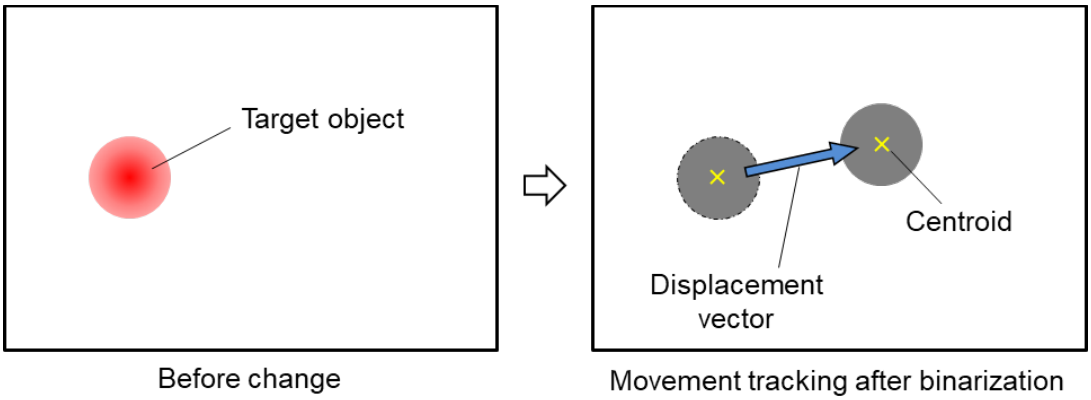

Fig. 40. Schematic illustration of movement tracking by using the centroid of binarized image.

The ground glass location effect is also checked for the binarization technique. The same set of images is used for the 2D DIC is used for the comparison between the techniques. The shape of the binarized image and the calculated centroid for a few threshold levels is shown in Fig. 41. When the threshold gets larger, the size of the binarized object gets smaller since the intensity at the center is larger than the surface.

The tracking results as a function of threshold levels are shown in Fig. 42. The binarization method shows that the lower threshold value generates a smaller error, which is less than 0.3 px. The location effect gets larger for the large thresholds since the beams are more distorted.

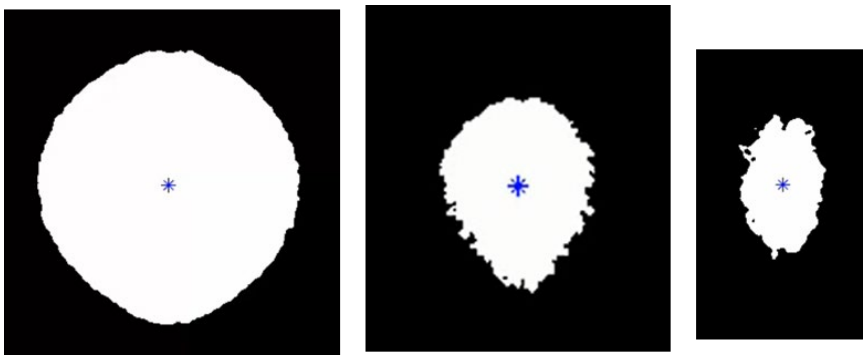

(a) (b) (c)

Fig. 41. The binarized image of the beam for (a) threshold = 1, (b) threshold = 30, and (c) threshold = 50, and the blue symbol shows the centroid of the object.

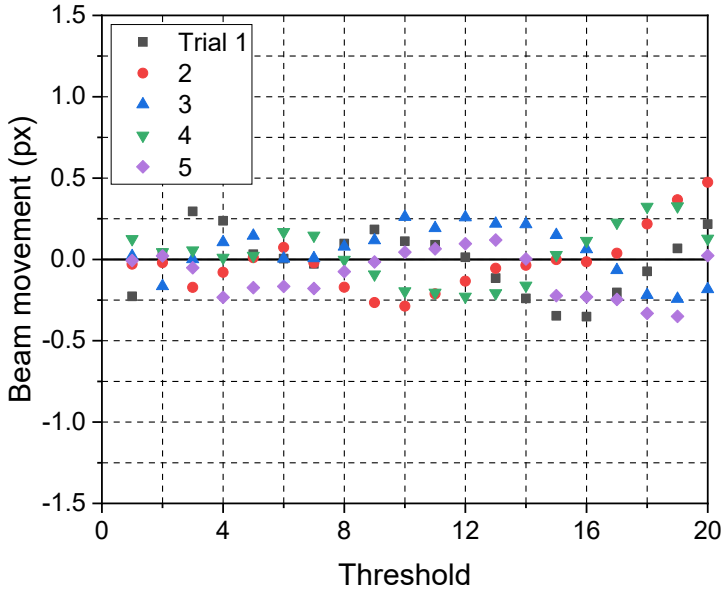

Fig. 42. The tracking results of the binarization method for each trial as a function of threshold value.

The result clearly indicates that the binarization method shows less location effect. As mentioned earlier, the intensity distribution of the beam changes when the

ground glass is moved, and the DIC cannot track the beam with a good correlation since the distribution randomly changes. For the binarization method, the light near the threshold level is affected by the location effect, but the effect is much smaller.

The selection of the tracking method should be done considering the characteristic of the object and the performance of the tracking. The tracking performance can be quantified by conducting a test where the amount of the movement is known, like the ground glass location effect test. For the tracking of the laser beam movements projected to the diffusive optical target, the binarization method could improve the performance of the tracking significantly.

As an additional step to check the binarization method, the ground glass location effect is checked for the beam after being reflected by the reflective Aluminum surface to make the test closer to the actual measurement. Fig. 43 shows (a) the schematic diagram of the setup, (b) the image of the beam, (c) intensity of the beam, and (d-f) the binarized beam image for the threshold 1, 20, and 50. It is clearly seen that the beam shape is distorted compared to the direct illumination case. Similar to the previous case, the 0.5 mm movement of the ground glass is repeated 5 times. Fig. 44 shows the result of the beam tracking, and the location effect less than 1 pixel is observed. The expected movement of the beam during the warpage measurement is tens of pixels, and the expected error caused by the ground effect is a few percent.

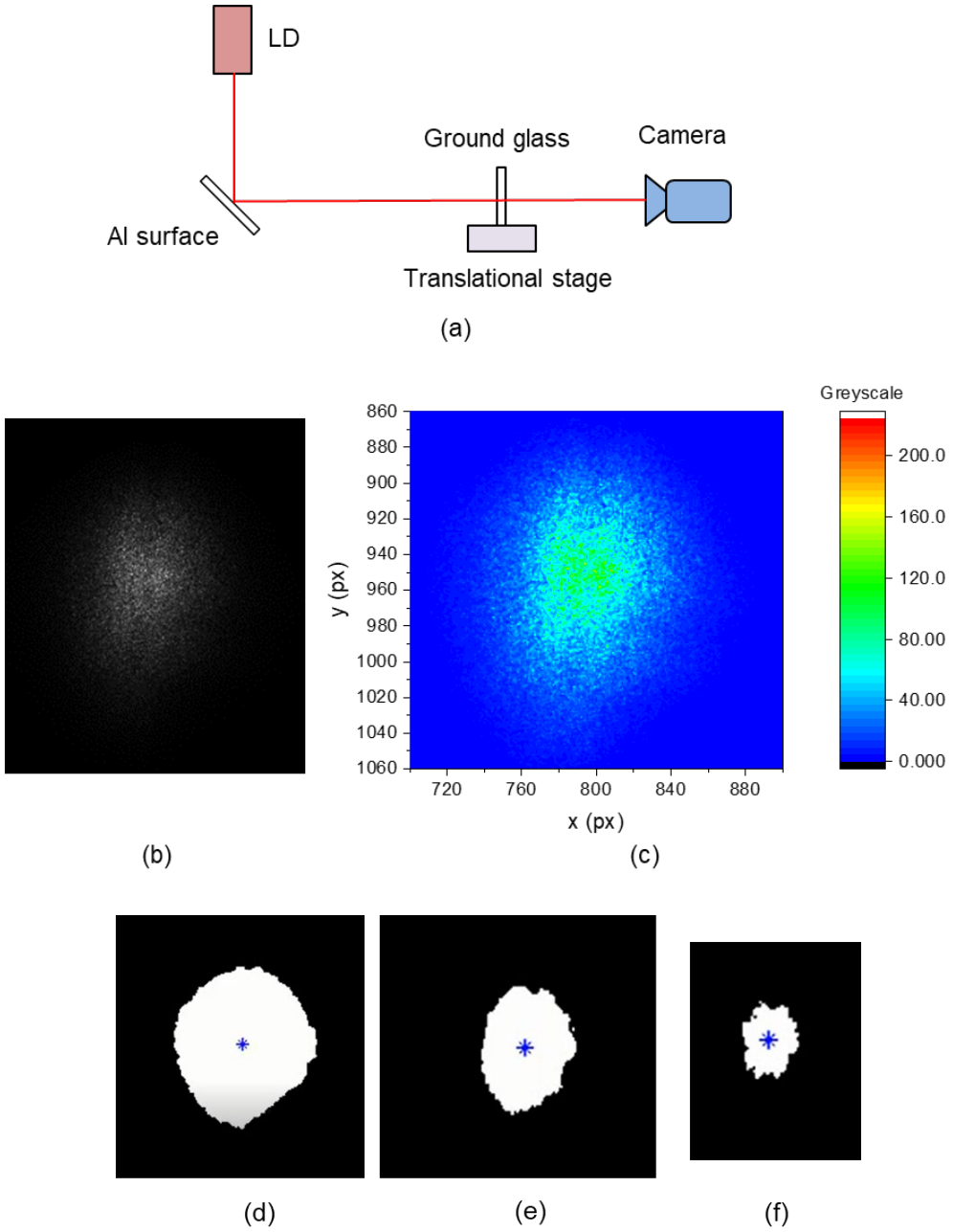

Fig. 43. (a) Schematic of the setup to check the location of the reflected beam, (b) image of the beam, (c) intensity distribution, (d-f) binarized beam for the threshold 1, 20, and 50, respectively.

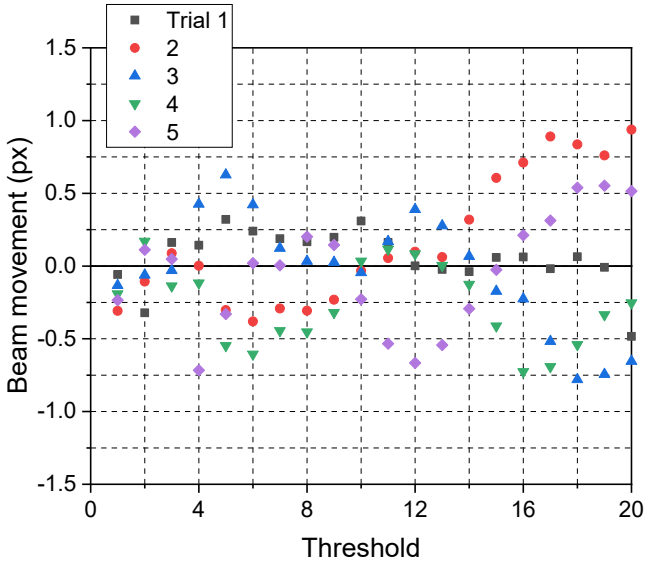

Fig. 44. The results of the beam movement generated by the location effect of the reflected beam.

3.3. Development of Test Setup

The bimaterial specimen, mold, and optical setup are designed and fabricated for testing. After examining the characteristics of the laser beam, some auxiliary tests are conducted to establish the measurement accuracy and stability while evaluating the uncertainties.

3.3.1 Fabrication of bimaterial specimen

A round bimaterial specimen is illustrated in Fig. 45, which consists of a substrate and EMC. Commercially available Aluminum disk was used as a substrate. The surface was polished to produce the required surface smoothness for the test.

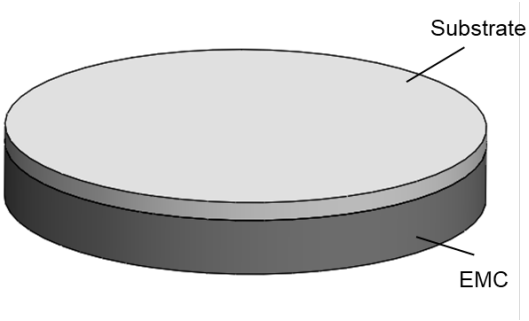

Fig. 45. Schematic illustration of the bimaterial specimen.

Since the amount of ECS is in the range of hundreds of microstrain, and the modulus of the substrate is much higher than the EMC, the thickness and diameter of the substrate as well as the thickness of EMC was carefully selected using a supplementary numerical analysis while considering availability of Aluminum disks. The final specimen diameter was 25 mm, and the thickness of Aluminum and EMC were 1.0 mm and 3 mm.

An Aluminum sheet with a 1.0 mm thickness was cut into a disc shape by using a waterjet cutting (ProtoMAX: OMAX). The surface was then polished by using the particle size as small as 0.5 μm. The thickness variation of the substrate after the polishing was less than 10 μm.

3.3.2 Mold and optical setup design

The mold and pressure application system were designed to achieve the requirements for the warpage measurement. A custom-designed Aluminum mold is shown in Fig. 46.

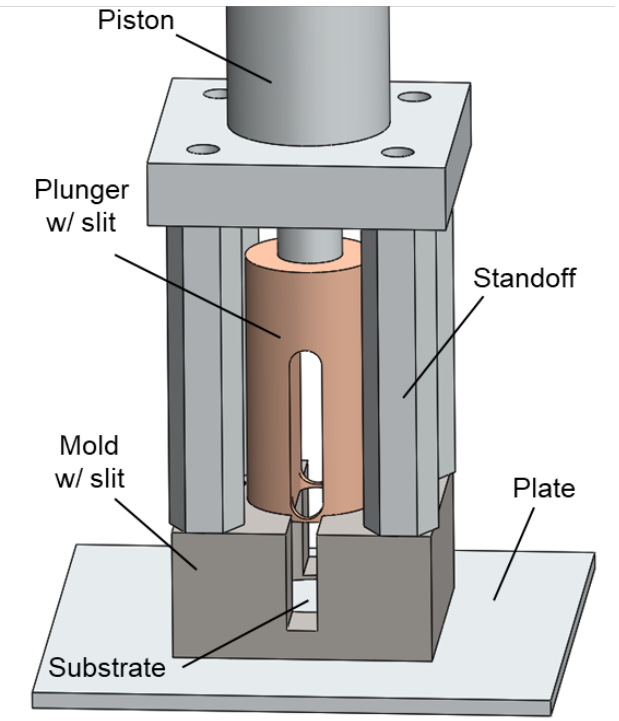

Fig. 46. Schematic diagram of the experimental setup including mold.

There is a hole at the center of the mold, and the diameter is slightly larger than the diameter of the specimen to achieve sliding fit. There is a slit along the sides of the mold to allow the laser beams. The bottom part is slightly longer than the specimen thickness to prevent EMC leakage during pressure application. The bottom part of the mold is sealed through an Aluminum plate, which is fixed to the conduction heater (HCP304SC: INSTEC). A mold release agent is applied where the specimen touches so that the EMC can be separated from the mold without constraints.

The pneumatic piston (121DV: BIMBA) is placed on top of the mold, and the piston body is connected to the mold by using standoffs. A pressure regulator (ER5000, TESCOM) is directly attached to the piston, which can apply the maximum pressure of 100 psi. A plunger is attached to the tip of the piston, and the diameter of the plunger

is slightly smaller than the inner diameter of the mold so that the plunger can move vertically while minimizing tilting. The plunger also has a slit at the side and the bottom of it to allow the beams to pass while the plunger touches the specimen. The schematic diagram of the laser beams passing through the mold is shown in Fig. 47.

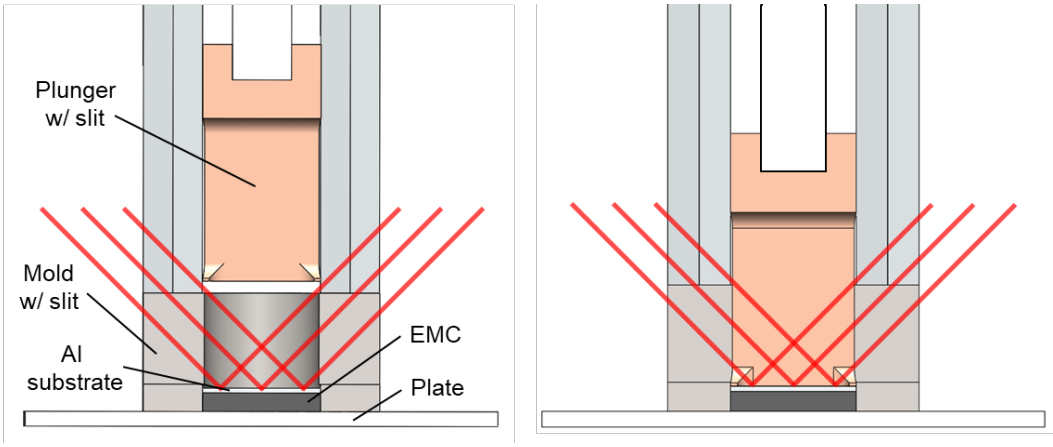

(a) (b)

Fig. 47. The schematic diagram of the laser beam passing the mold (a) while the plunger is lifted, (b) plunger presses the specimen.

The collimated LD (COL-20G-640: World star tech) with the maximum intensity of 20 mW was used for the system. The beam shape is elliptical, and the size of the beam is 5 × 2.1 mm. The beam divergence is less than 1 mrad, and the center wavelength is 640 nm. The size of the collimated laser diode unit is 8 mm (D) × 12.8 mm (L), which is small enough to be attached to a rotational and translational stage installed above the optical table surface, as shown in Fig. 48. The input current is controlled by using a sourcemeter (2401: KEITHLEY). The intensity of the light was measured by using a power meter (LaserMate-Q: COHERENT), and the output as a

function of the input current is shown in Fig. 49, where the threshold current is 47 mA. In the current range above the threshold level, the relationship between the input current and the output intensity is linear ($R^2 = 0.9999$), as shown in Fig. 49 (b).

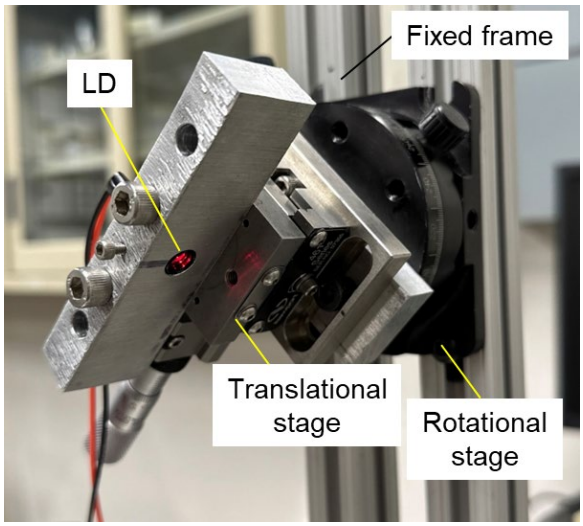

Fig. 48. Laser diode attached to a tunable stage above the optical table.

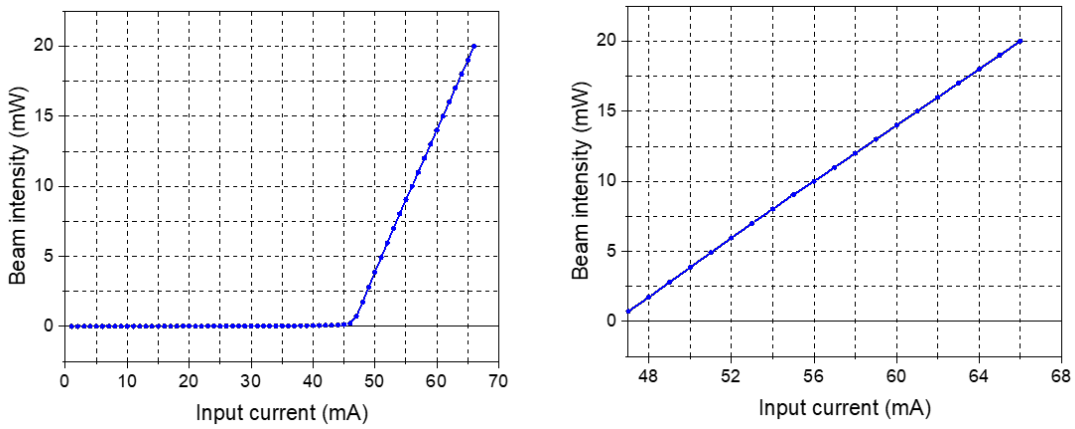

(a) (b)

Fig. 49. Intensity of the beam from LD as a function of input current; (a) entire input current range, (b) input current above threshold.

Five beams were used for the warpage measurement, considering the size of the specimen and LD beam. The beams were evenly distributed along the centerline of the specimen by using a glass with a thickness of 5.9 mm. The middle beam (beam 0) was located at the center of the specimen. The locations of other beams were -2/3, -1/3, +1/3, +2/3 of the specimen radius, and they are named beam -2, -1, +1, and +2, respectively. The 2^{nd} beam has the highest intensity, and the -2^{nd} beam has the lowest intensity.

Both sides of the glass plate were coated with Aluminum using a high vacuum evaporator (DV 502: Denton Vacuum). The Aluminum coating was controlled to produce a desired reflectance of R = 0.85.

The beams reflected from the specimen surface were impinged on a ground glass diffuser (50 × 50 mm, 600 grit: Edmund Optics). The transmitted light after passing through the ground glass was captured by a 2/3" format CCD camera (GS3-U3-28S5M: Point Grey Research) and an imaging lens (Zoom 7000: Navitar). The CCD sensor has 1920x1440 pixels, and its frame rate is 26 frames per second.

As mentioned earlier, the input current for each beam has to be adjusted during the warpage measurements. The linear relationship of the input current and the laser diode intensity, and the theoretical calculation of the intensity of the transmitted beam after the multiple reflections were presented before. In the actual experiment, the absorption of the coating should also be considered for the correct input current values. A flow chart used to automatically determine the input current for each beam is shown Fig. 50 (a). The average beam intensity was used as a criterion to determine appropriate

current values. The average intensity variation among the beams of a grey level ± 0.5 was readily achieved through this process.

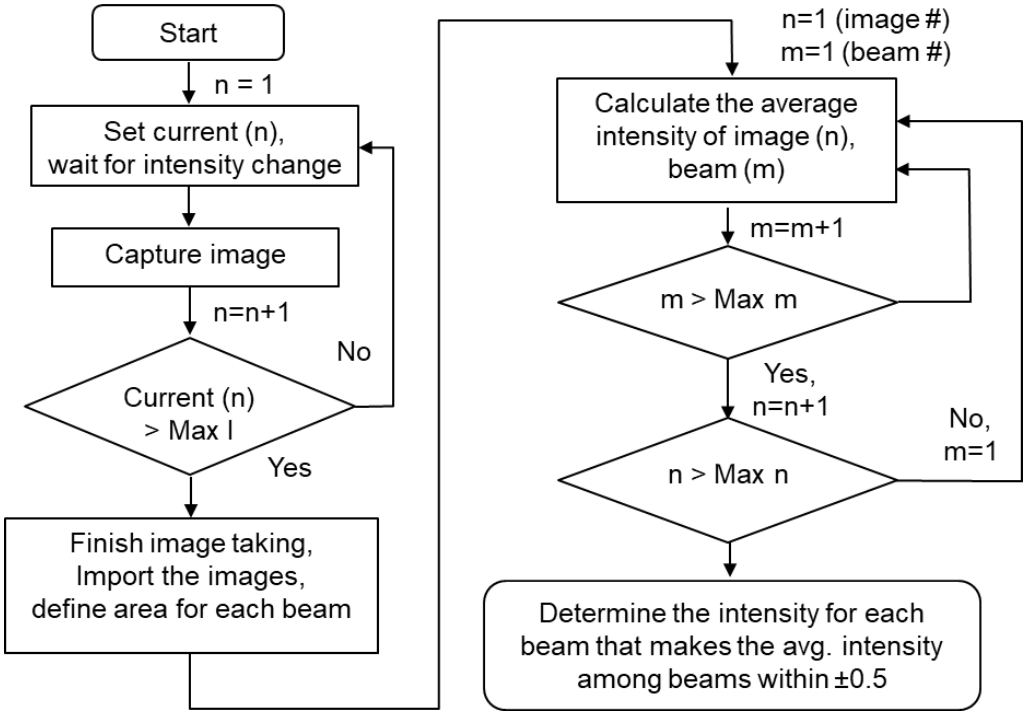

(a)

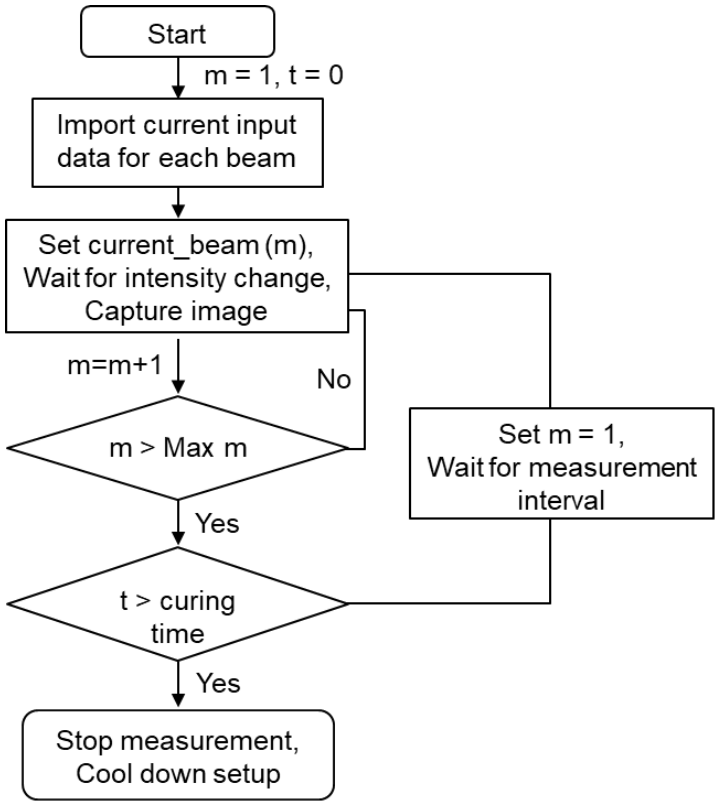

(b)

Fig. 50. Flow charts to (a) determine the input currents for beams, (b) change beam intensity and capture images for each beam.

An automatic image capturing routine was developed to capture the multiple beams quickly after the required current value for each beam is determined. The flow chart used to develop a LabVIEW program for this routine is shown in Fig. 50 (b). The current hardware causes a time lag of 0.3 second for the input current control. Five beams were used for the implementation, and each set of five images was captured in 1.2 seconds. The actual LabVIEW program is shown in Fig. 51. This automatic and fast image acquisition is critical to successful measurements as the warpage changes rapidly after the mold pressure is removed.

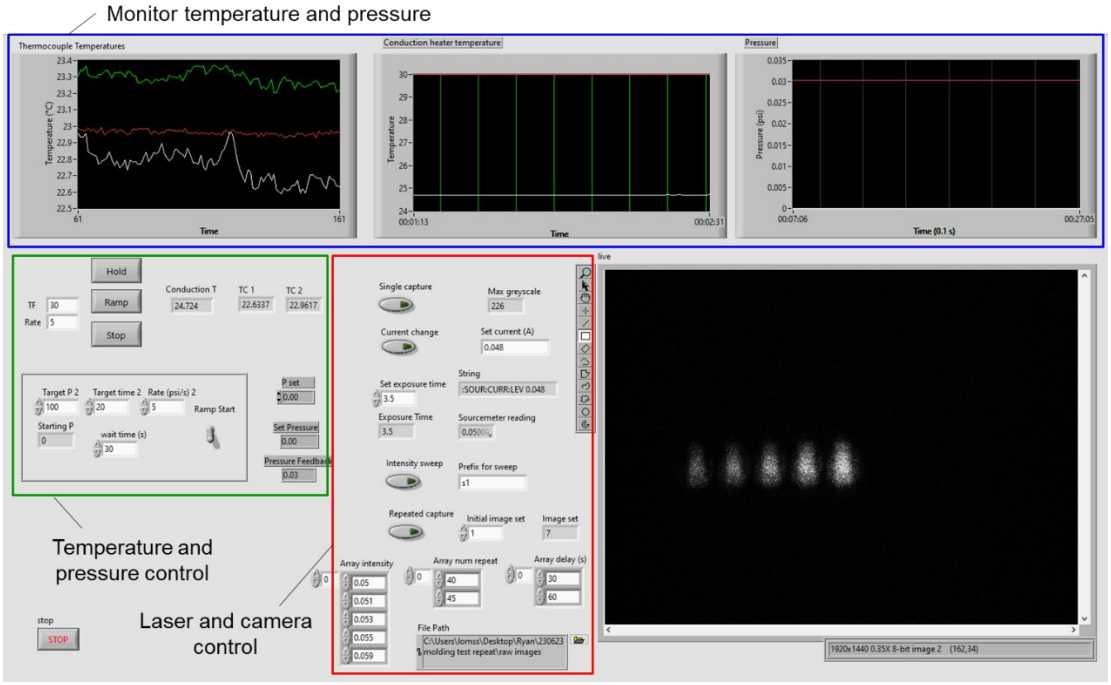

Fig. 51. Capture of LabVIEW program for the warpage measurement; the red box part controls the laser intensity and captures image systematically.

3.3.3 Evaluation of optical/digital setup

The accuracy of optical/digital setup was evaluated. The schematic diagram of the configuration used to evaluate the setup is shown in Fig. 52 (a). The Fabry-Perot based multiple-beam generation produced five beams. They were reflected from a reflective plate and were projected on the optical target (ground glass). As illustrated in the figure, a shim with a thickness of 112 μm was inserted under the corner of the plate, which caused the plate to be tilted by 0.069°.

The five beams obtained using a constant current is shown in Fig. 52 (b). As expected, the intensity of the beam decreased extremely rapidly, and the 5th beam was

barely visible. The program based on the flow charts in Fig. 50 was executed, and a new set of 5 images are shown in Fig. 52 (c).

The input current used for each beam and the average beam intensity are plotted in Fig. 53. The average beam intensity obtained from Fig. 52 (b) is also shown. The enhancement is clearly evident.

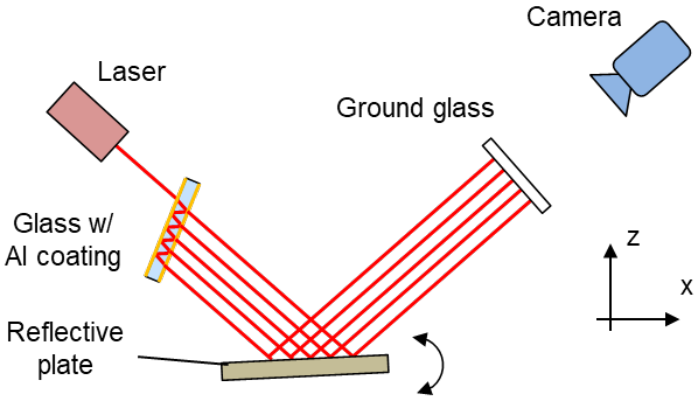

(a)

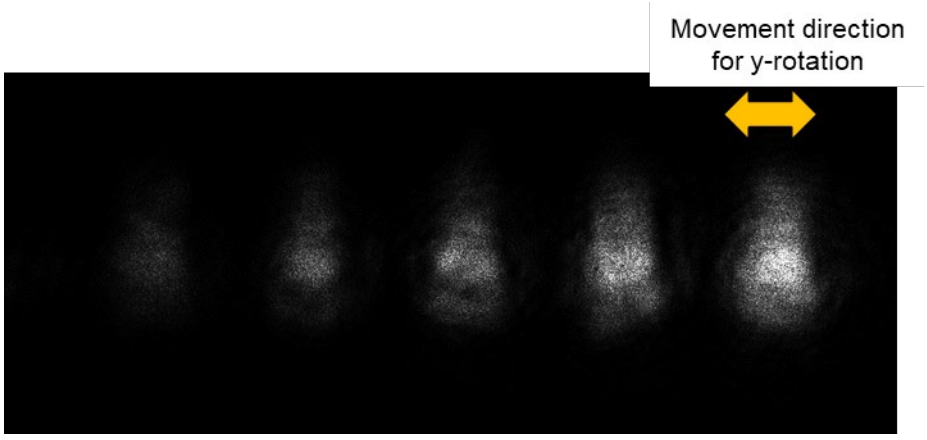

(b)

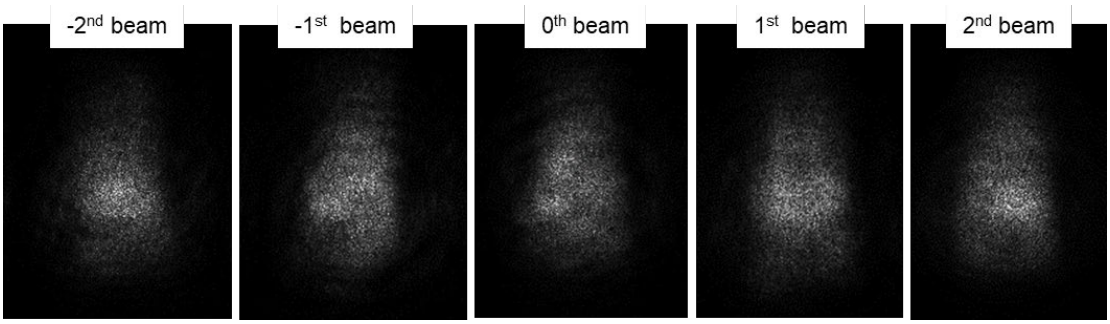

(c)

Fig. 52. (a) Schematic diagram of the testing setup, (b) multiple beams captured by the camera, (c) images of each beam with the same average intensity.

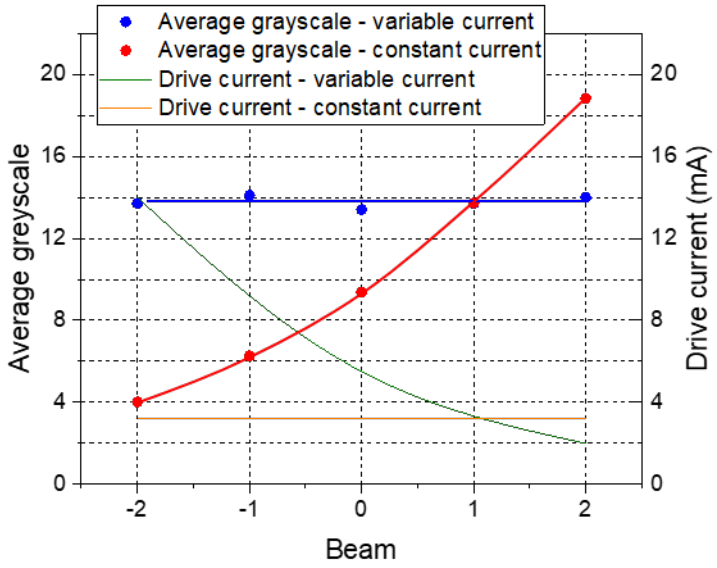

Fig. 53. The input current used for each beam tracking, and the average greyscale of each beam; the case for variable current and constant current are shown.

The proposed binarization-based tracking method was implemented for the enhanced beams. The results are shown in Fig. 55, where the horizontal line represents the slope produced by the shim. The threshold for the beam movement tracking was

determined based on the tracking stability. When the threshold is too low, the beams are not separated properly. On the other hand, if the threshold is too high, the beam shapes are distorted. Considering these two effects, the threshold of 15 was selected for the tracking.

The tracked beam movement for 5 trials are shown in Fig. 54(a). The tracked movements are consistent, and the error between the trial was up to 1.3 px. The shim stock with the thickness larger than 100 μm is used to generate the rigid body motion, and the amount of the z displacement was not negligible, and it generated the beam movement up to about 3 px. The movement generated by the z displacement was larger for the higher order of the beam, and $+2^{nd}$ beam has about 1 px larger movement than -2^{nd} beam. The z displacement effect was removed from the beam movement before the slope measurement, and the adjusted beam movement is shown in Fig. 54(b).

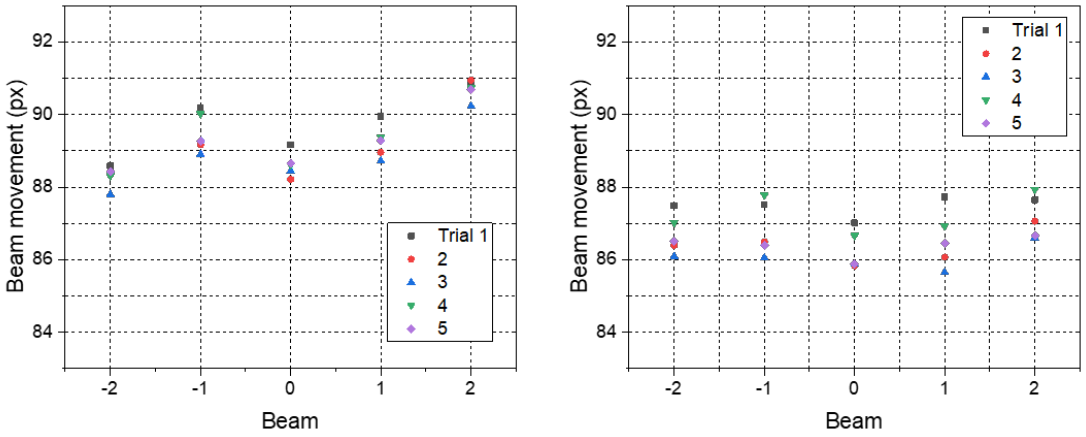

Fig. 54. Results of (a) raw beam movement for 5 trials, (b) adjusted by the z displacement due to the thickness of shim stock.

The slope is calculated based on the beam movement by using the governing equation Eqn. (16). The angle calculation results are shown in Fig. 55(a). The horizontal line shows the theoretical movement, and the results show that the measurements are very closer to the theoretical value. The theoretical pixel movement is the calculated pixel movement based on the angle change (0.069°). The measurement data is different by up to 0.0012 °. Then, the curvature is determined by using the slopes of the beams for each trial. Since the rigid body rotation is applied, the theoretical curvature is 0. The result is shown in Fig. 55(b), and the virtually 0 curvature indicates that the beam movement was generated by the rigid body motion.

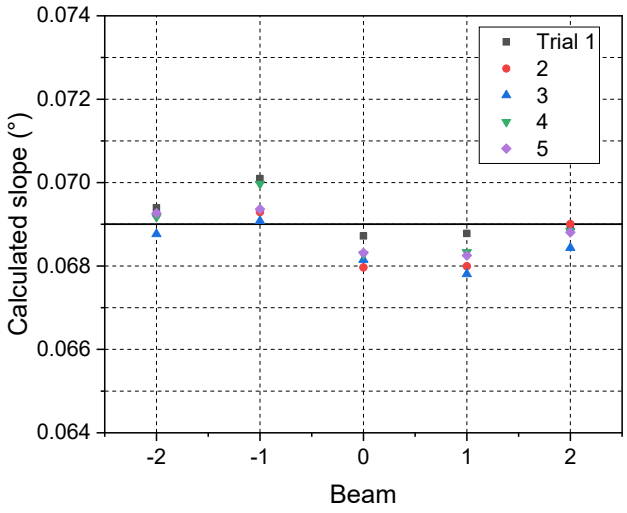

(a)

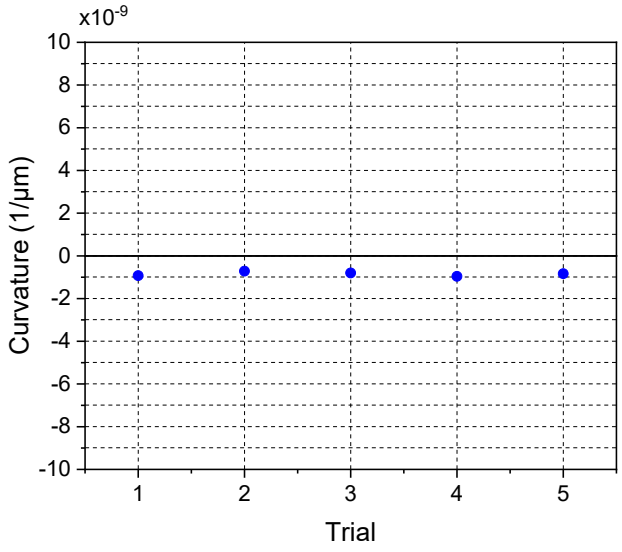

(b)

Fig. 55. (a) the calculated slope changes by the rigid body rotation in y axis, and (b) curvature of the beam movement.

3.4. Results of in-line warpage measurements

The test procedure is explained in detail, and the result of the measurement is presented. The test is repeated to check the accuracy of the measurement. The effect of the rigid body motion and the effect of the beam reflection from the substrate surface are discussed.

3.4.1 Test procedure

The pellet form of EMC was first prepared in a powder form to make it closer to the specimen shape before the testing is started. A polyimide tape is wrapped around the side of the aluminum substrate and EMC, and a very small amount of the silicone elastomer was added to the corner of the substrate to prevent leakage during the

pressure application. The substrate and the EMC were inserted into the mold, and the bottom of the mold was closed by fixing it to the bottom plate, which was connected to the conduction heater.

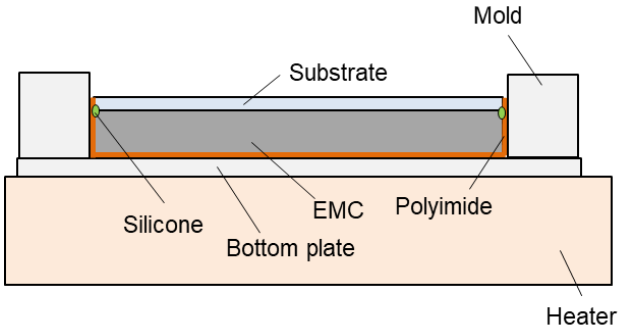

Fig. 56. Schematic illustration of the parts near the specimen

The piston was attached to the pressure regulator, and they were connected to the mold like previously shown in Fig. 46. The alignment of the plunger with the mold was examined by moving the plunger up and down. When the insulation layer was added around the mold and heater, the laser beams were also examined to check if the reflected lights were detected clearly by the camera. The 5 laser beams (-2^{nd} , -1^{st} , 0^{th} , $+1^{st}$ and $+2^{nd}$) were adjusted in such a way that the 0^{th} was landed on the center of the specimen. The laser diode location is adjustable by using the translational stage like shown in Fig. 48, and the center of the specimen was found by adjusting the location of the beam on the specimen. A small amount of pressure (0.03MPa) was applied to the specimen to prevent unwanted movement during heating.

The conduction heater has a very fast ramp rate, and the temperature within the setup becomes non-uniform when the heating is done fast. The preheating is done before heating to the mold temperature like illustrated in Fig. 57. By preheating, the

temperature variation can be minimized while heating to the mold temperature. While heating to the mold temperature, pressure is applied and removed before passing the gel point. At the mold temperature in the transfer molding, the molding compound cures rapidly, and quickly passes its gel point, at which the molding compound becomes a deformable solid. As a result, the pressure to fill the cavities is no longer transferred to the molding compound in the cavities after the gel point, although the pressure is maintained until the mold is opened for removal of the encapsulated components. To simulate this condition, the mold pressure should be removed before passing the gel point. After the temperature reaches the mold temperature, the measurement is started.

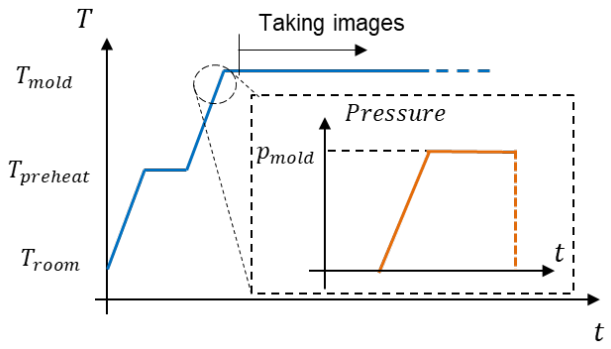

Fig. 57. Schematic illustration of the temperature and pressure profile during the warpage measurement.

The temperature and pressure profile during the test are shown in Fig. 58. The setup was preheated to 80°C first because the curing rate of EMC at that temperature is negligible, and then it was heated to the target temperature, 120°C. The T_g of the EMC determined by using the DSC is 130°C, but the mold temperature is set to be 10 °C lower than that to make sure the EMC does not pass the gel point when the specimen

is heated to the mold temperature. The *x*-axis shows the time for the measurement; i.e., time = 0 is when the first measurement was made. When the mold temperature reached 105°C, 1.1 MPa of pressure was applied at the rate of 0.05 MPa/sec. The pressure was maintained for 30 seconds, and the plunger was lifted to remove the pressure completely. After the temperature reached the mold temperature, the images of the beams were taken at every 30 seconds. The exposure time of the camera was 2 ms, which was sufficiently short to avoid any noticeable image change (i.e., blurry image) while taking all five images.

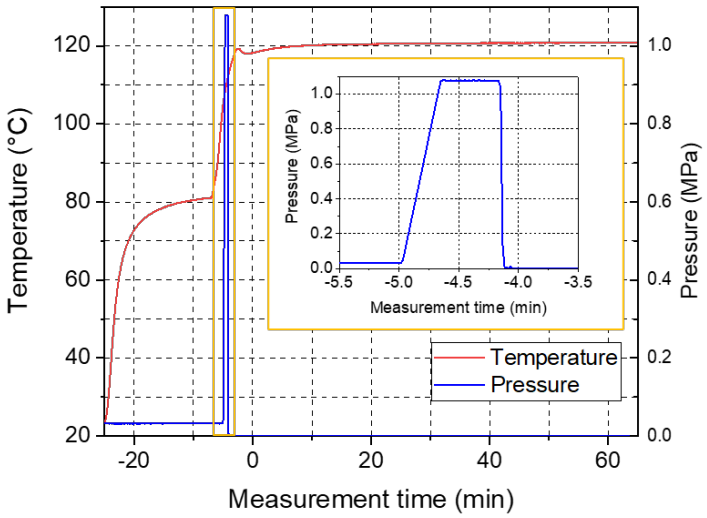

Fig. 58. Temperature and pressure profile during the measurement. The inset shows the application and removal of the pressure.

A supplementary test using DSC was conducted to determine the warpage test duration prior to the actual warpage measurement. The DSC result based on the isothermal mode is shown in Fig. 59. The result indicates that the curing is expected

to be completed (> 98%) after 1 hour. Based on this, the warpage measurement was conducted only for an hour.

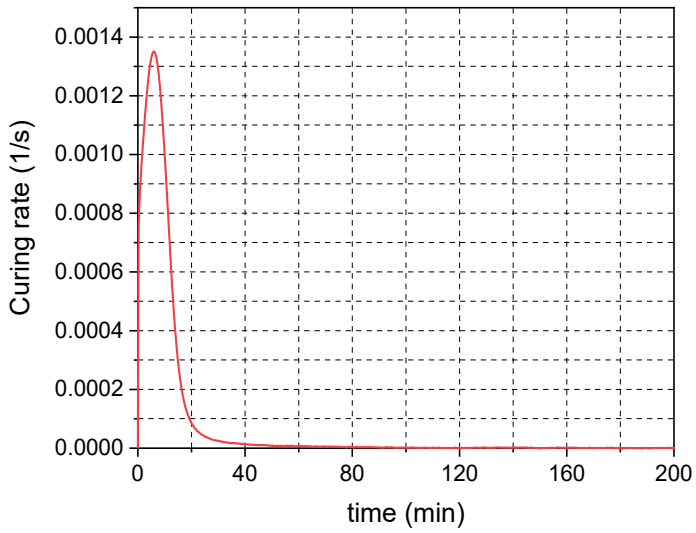

Fig. 59. Isothermal curing data of EMC at 120°C.

3.4.2 Test results

The configurations of the specimen and optical target are shown in Fig. 60. The 5 laser beams are evenly distributed along the centerline of the specimen. The reflected beams are projected to the ground glass, and the camera captures a portion of the ground glass where the beams are projected.

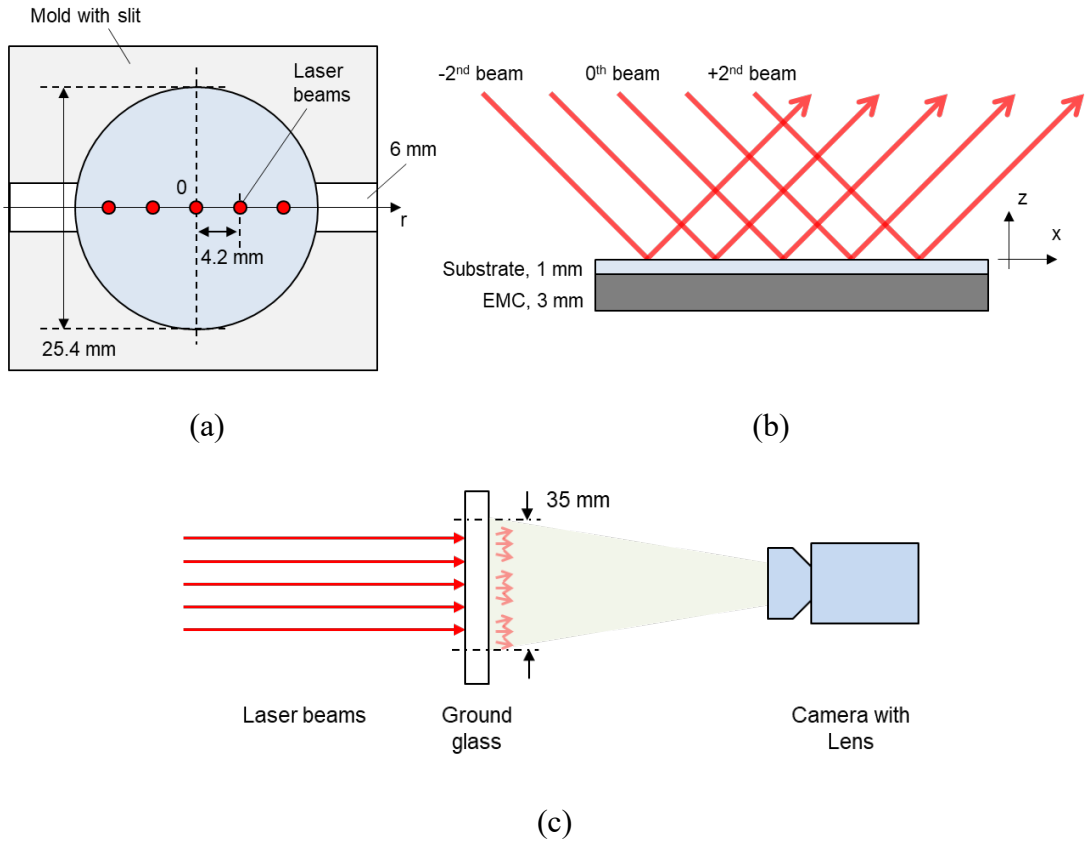

Fig. 60. Illustration of the laser beams illuminated to the circular bimaterial specimen from (a) top view, (b) side view, and (c) the camera captures the image of the laser beams projected to the ground glass.

The input current used for each beam tracking is shown in Fig. 61. The average greyscale is also shown in the figure. The variations in the average greyscale values are less than 0.5. The intensity profile of each beam obtained using the variable current is shown in Fig. 62. The shape of the beam looks different among the beams, but their shape is maintained during the measurement. As an example, the images taken for 0^{th} beam tracking as a function of time are shown in Fig. 63. The image shows that there was a relative motion of the beams. The 0^{th} beam, which is illuminated to the center of

the specimen, does not show a noticeable movement. The other beams, however, show the movements as a function of time.

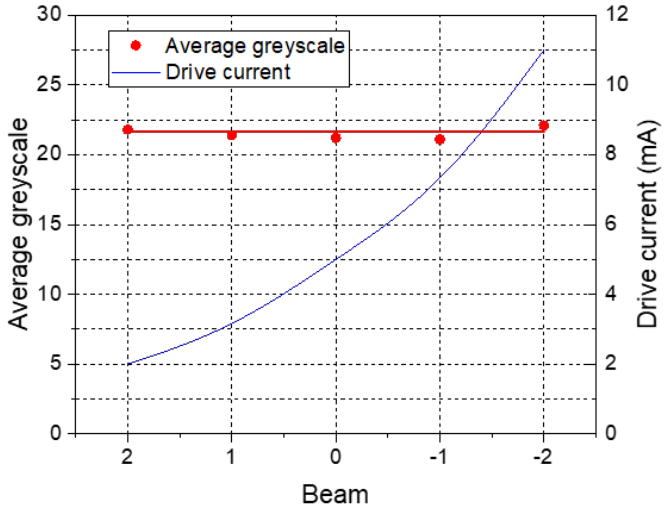

Fig. 61. The input current used for each beam and the average beam intensities.

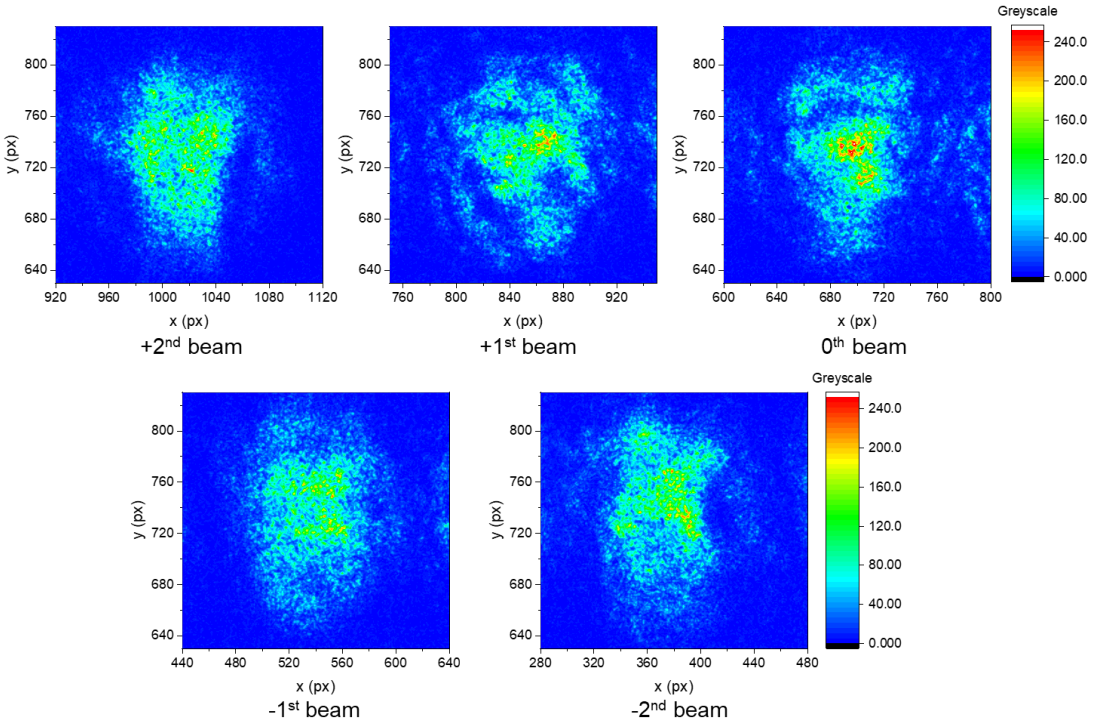

Fig. 62. The intensity profile of the beam when the average intensity is set to be the same.

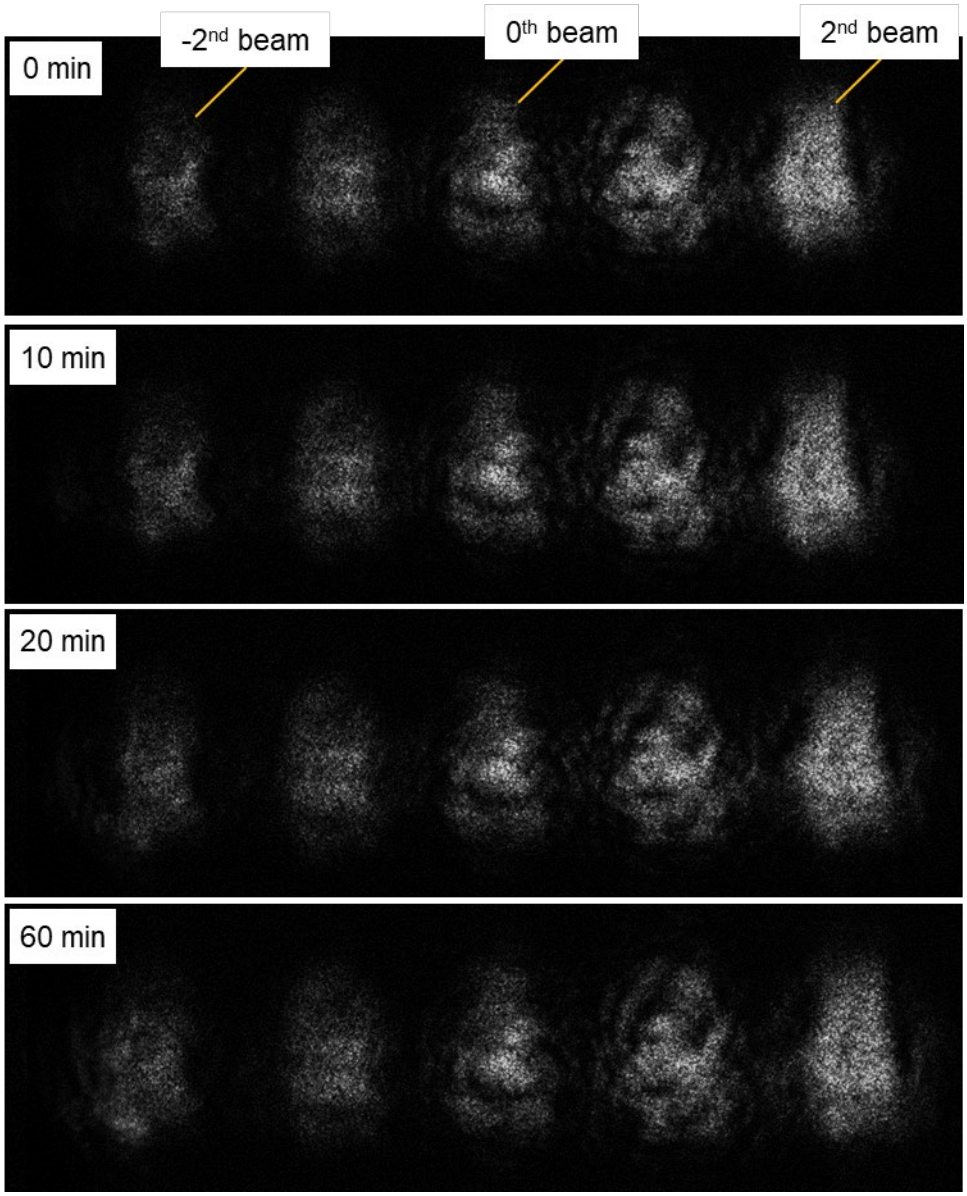

Fig. 63. Sample images of the beams as a function of time, the beams for the beam 0 tracking are shown.

The movements of the beams were tracked by the binarization-based tracking method. The beam tracking results as a function of time are shown in Fig. 64. The

incident angle of the beam was 45°, and the distances of the ground glass for the center beam (0^{th} beam) from the specimen surface were 474 x 474 mm. The angle of the ground glass was 45°, and the 1 pixel movement captured in the camera corresponded to 18.23 μm of the ground glass.

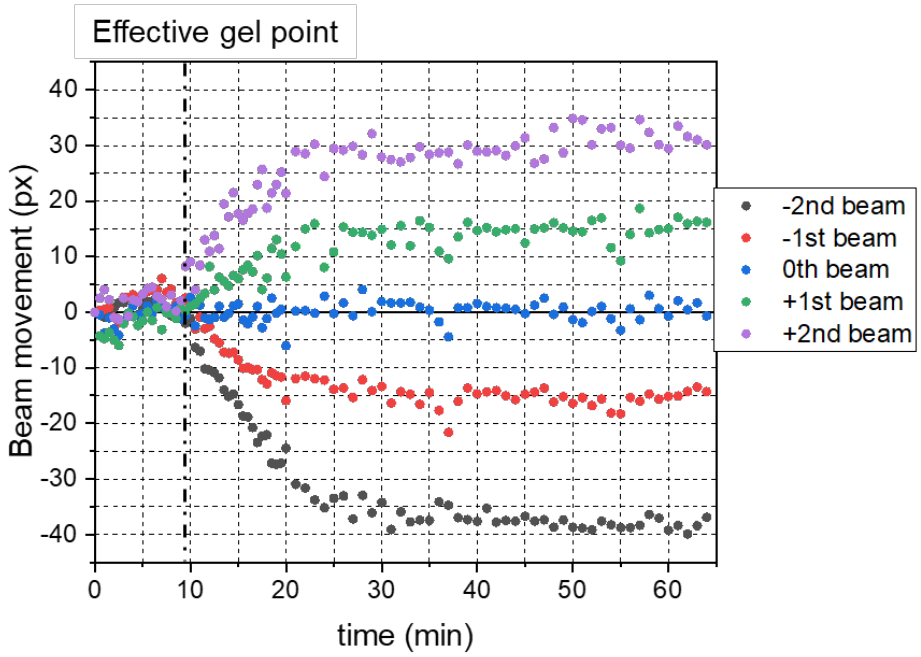

Fig. 64. Beam movement tracking results during the curing.

As discussed before, the residual stresses and thus warpage should not occur before the gel point. The beam movement began to occur around 10 minutes after the measurement started, which indicated the effective gel point. The beams moved continuously for approximately 40 minutes. No noticeable movements were observed after time ≈ 50 minutes. The slope of each beam determined by using the governing equation Eqn. (16). The calculated slopes are shown in Fig. 65.

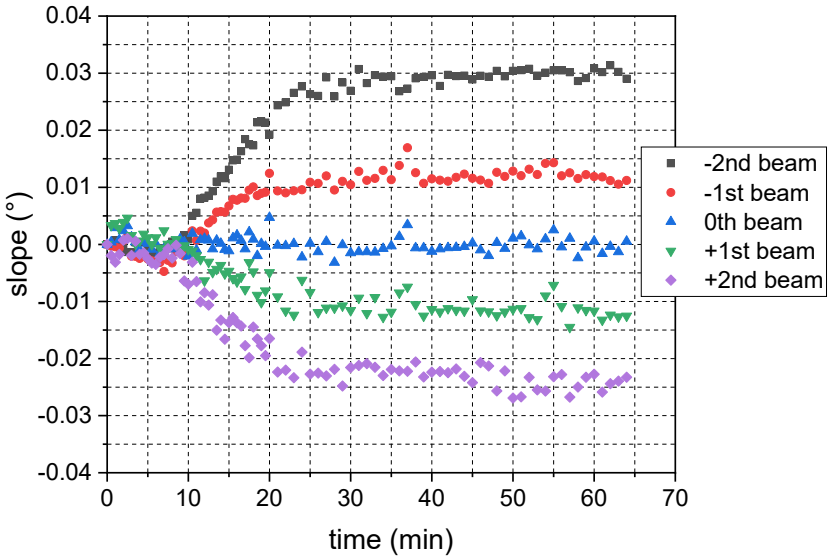

Fig. 65. The calculation result of the slope of each beam as a function of time.

The curvature is calculated by using the Eqn. (17) and, 5 slope values for each time step are used for the calculation. The linear regression was done to determine the curvature by using a linear equation $y = ax + b$. The slope calculated from the curvature is compared with the slope calculations in Fig. 66(a). The fitted line shows the good correlation with the slope values. The curvature for some representative time-steps is shown. The fitted line shows a nice correlation with the measured values, and $R^2 = 0.993$ at the end of the curing. The measured slope is almost symmetric since the lines in Fig. 66(a) passes near the center. The curvature changes during the curing are shown in Fig. 66(b).

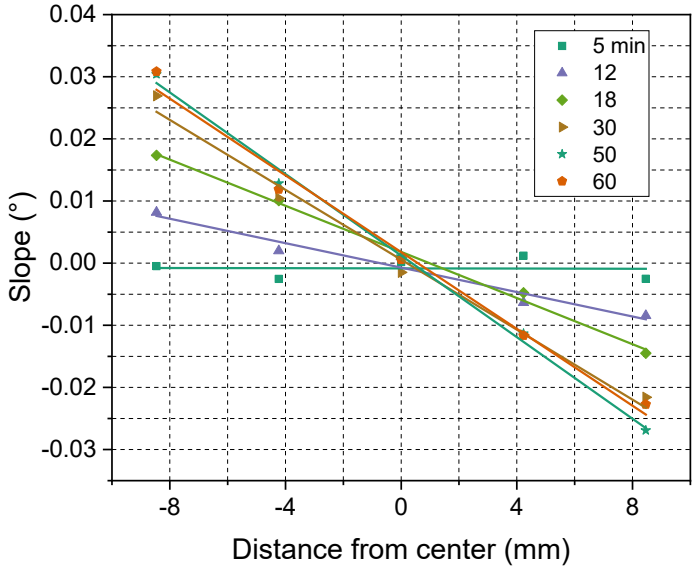

(a)

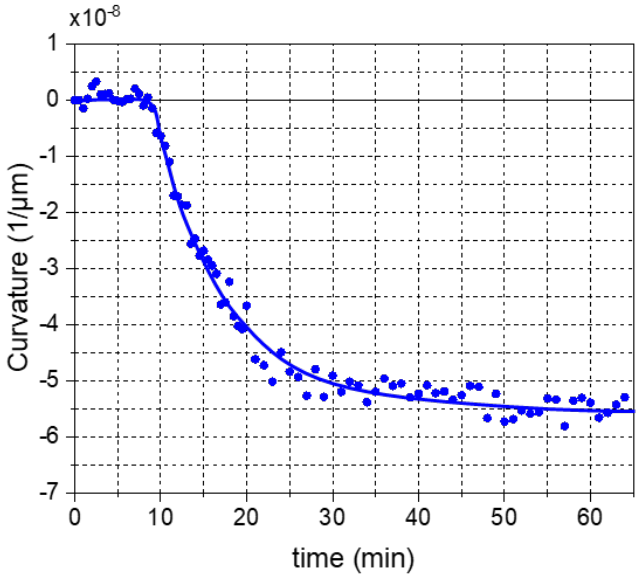

(b)

Fig. 66. (a) comparison of slopes from each beam movement (point) and fitted curvature (line), (b) result of curvature as a function of time.

The warpage is calculated for each time step by using the Eqn. (18), and the calculated warpage along the centerline of the specimen is shown in Fig. 67(a). The

time steps shown in Fig. 66 are shown. Fig. 67(b) shows the warpage at the point r/R = 1/3 and 2/3 as a function of time. The result clearly shows that no warpage occurs before passing the gel point, and the warpage change slows down as the curing continues. The measured warpage at the point of r/R = 2/3 (8.46 mm from the center) at the end of the curing is -2.0 μm.

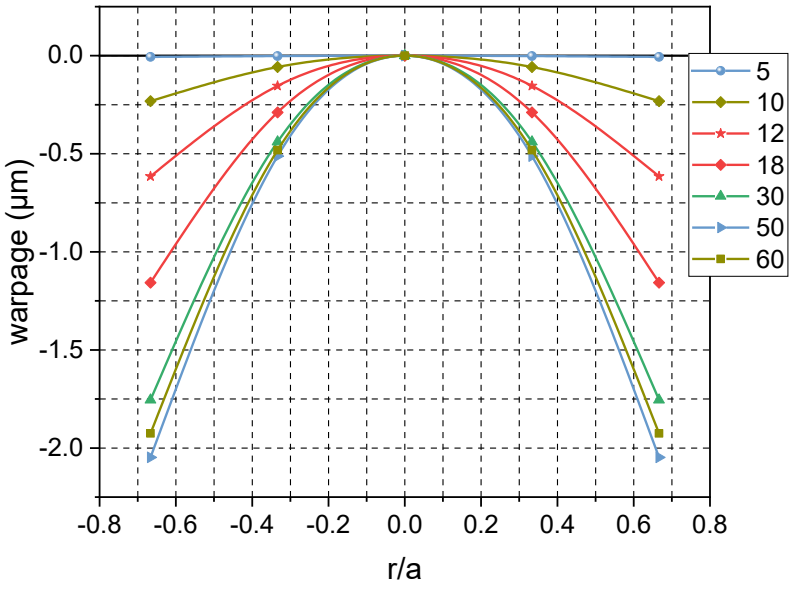

(a)

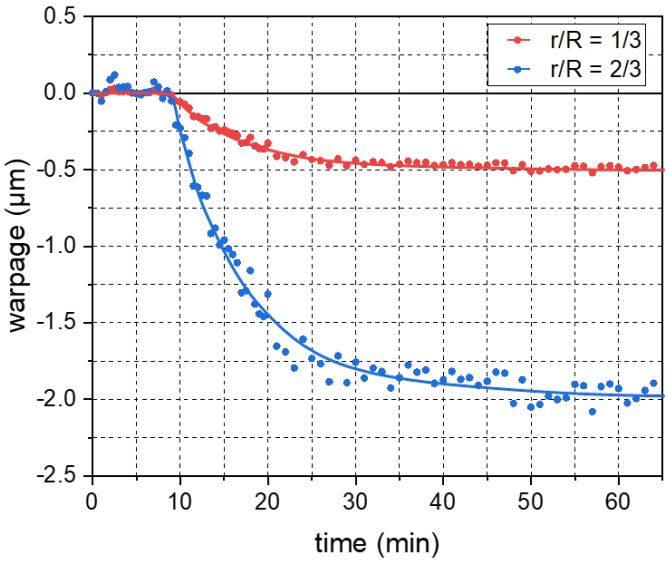

(b)

Fig. 67. Warpage calculation results during the molding process, (a) calculated warpage along the centerline of the specimen, (b) The warpage changes at the point r/R = 1/3 and 2/3 as a function of time.

3.4.3 Repeatability of the measurement

The warpage measurement was repeated to establish measurement accuracy and repeatability. The intensity profile of the beam and the beam movement during the test are shown in Fig. 68(a). The sample images for the 0^{th} beam tracking are shown as a function of time in Fig. 68(b). Similar to the original test, the beam movement except the 0^{th} beam can be seen.

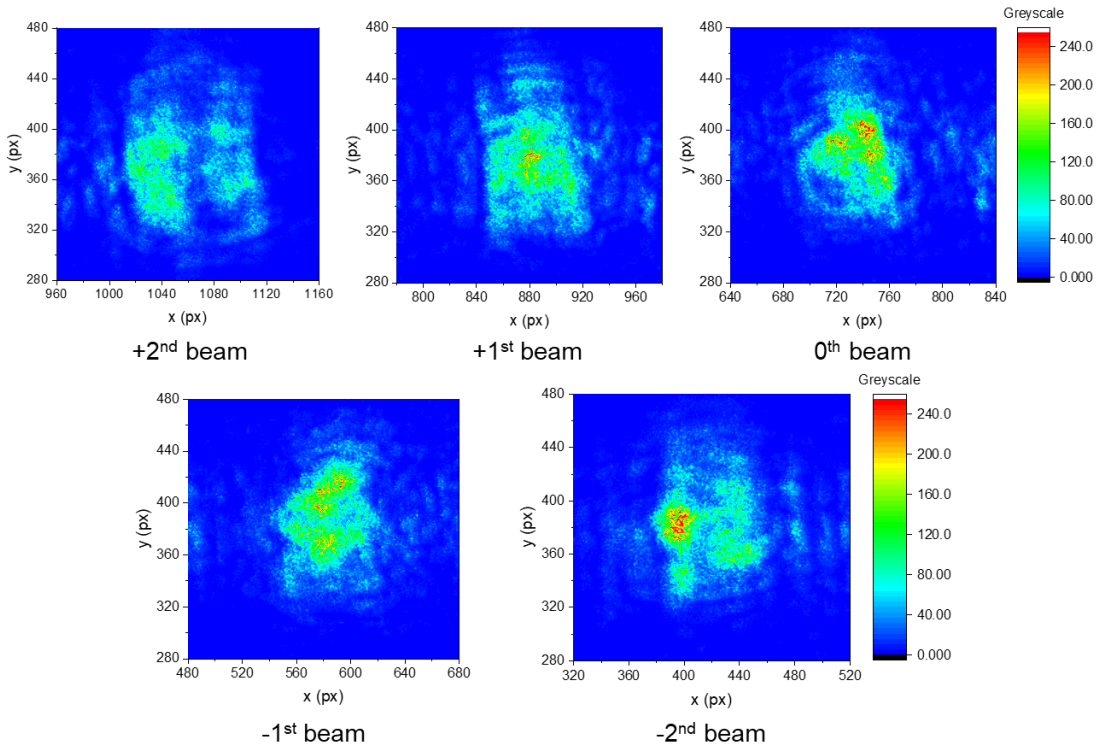
Greyscale
240.0
200.0
160.0
120.0
80.00
40.00
0.000
y (px)
x (px)
+2nd beam
+1st beam
0th beam
-1st beam
-2nd beam

(a)

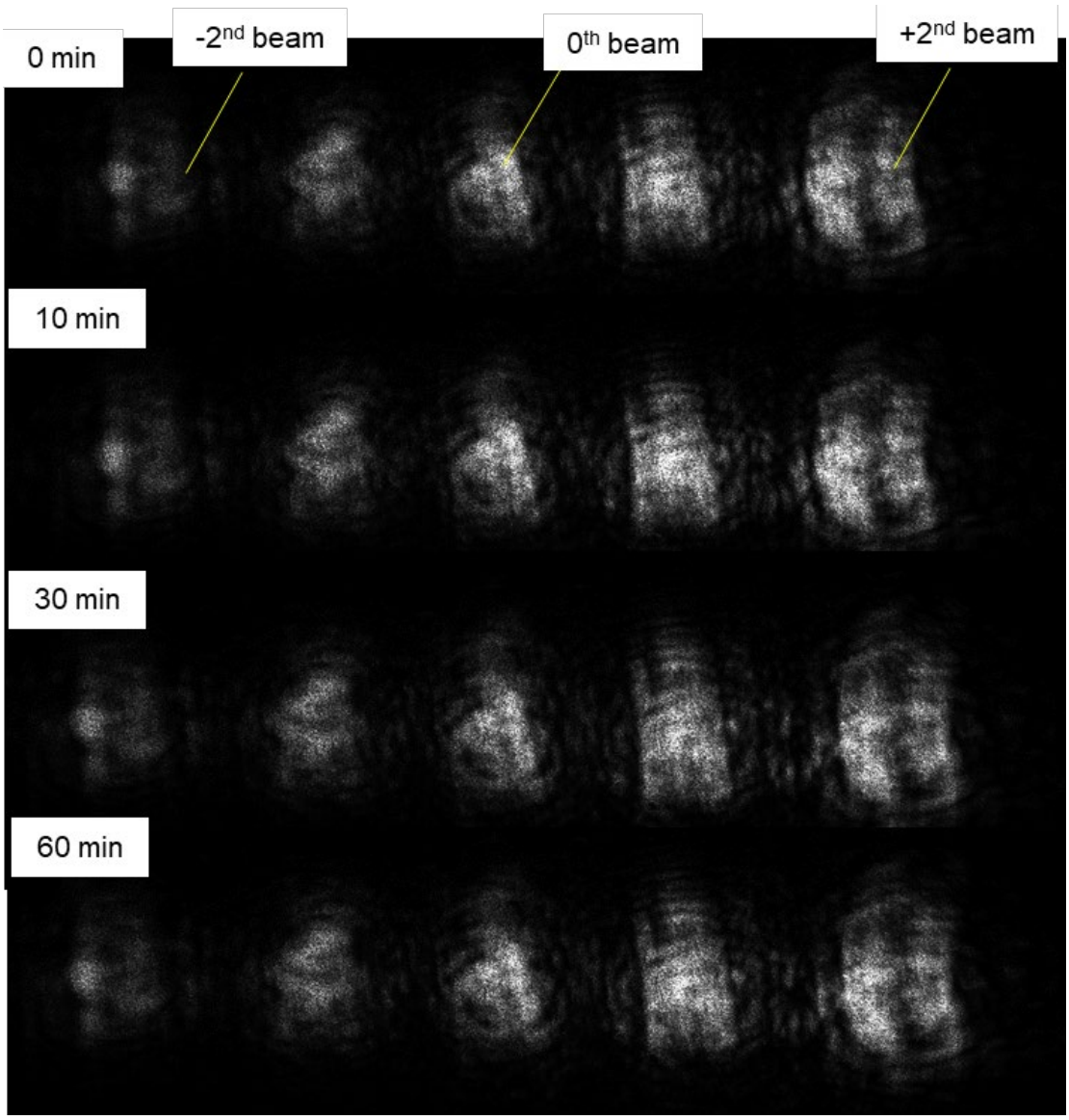

(b)

Fig. 68. (a) the intensity profile of the beam when the average intensity is set to be the same, (b) sample images of the beams as a function of time.

The beam movement results are shown in Fig. 69. The slope of each data point is compared in Fig. 70(a), and the calculated warpage value based on the slope is shown in Fig. 70(b). The results show that the measurement was repeatable since both the amount of the warpage and the trend of the warpage change are very close to each

other. The calculated warpage by using the curvature shown in Fig. 70(b) also shows the good match between two tests.

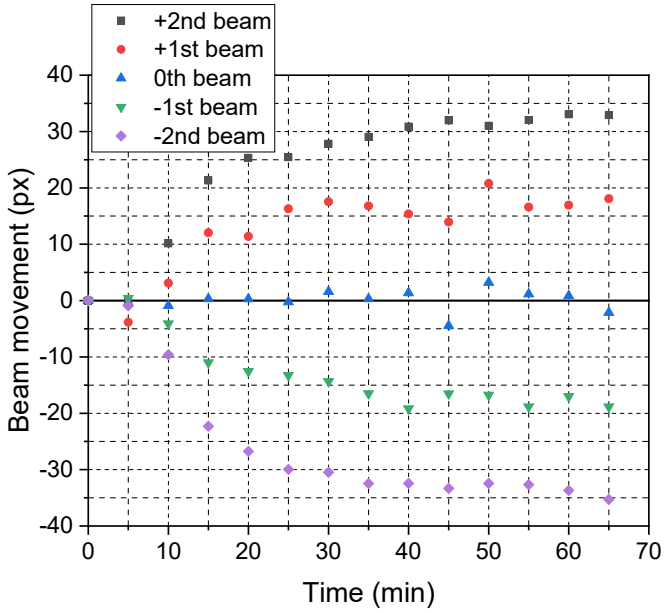

Fig. 69. The beam movement result of repeated test.

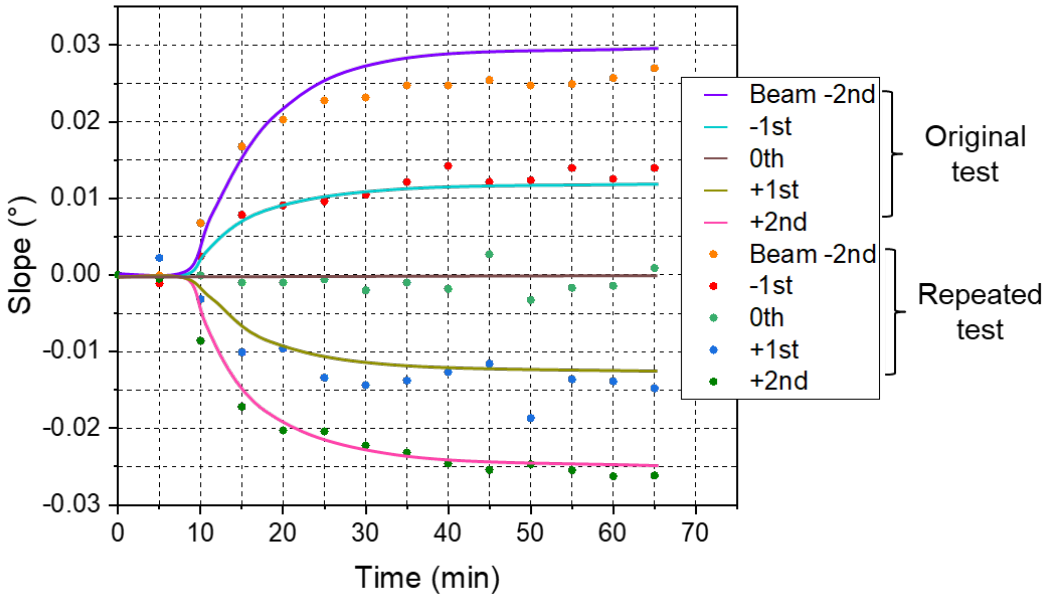

(a)

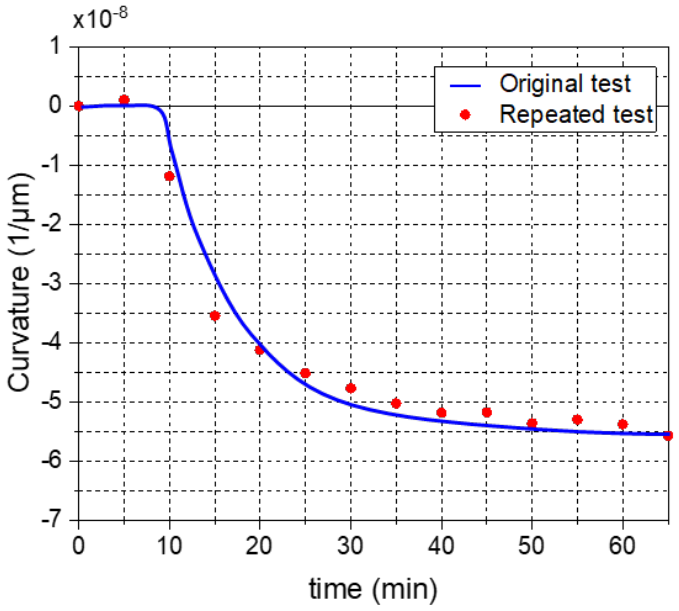

(b)

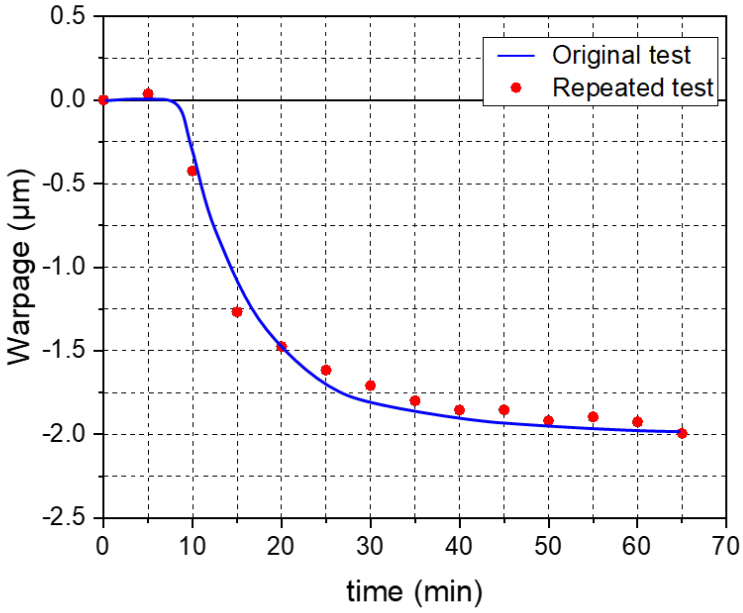

(c)

Fig. 70. The results of the repeated warpage measurement; (a) slope change, (b) curvature, (c) calculated warpage at the point r/R = 2/3 as a function of time.

3.4.4 Effect of rigid body motion in curvature calculation

In section 3.2.1, the governing equation to determine the slope and curvature of the specimen was developed. In the actual experiment, the movement can also be produced by accidental rigid-body rotation with respect to the *y*-axis and the deformation in *z*-direction. During the molding process, there are *z* displacement due to rigid body motion, height change due to effective cure shrinkage, and warpage generated. As briefly mentioned, however, the effect of those on the beam movement is very small for the warpage measurement test. As shown in the measurement result, the amount of the warpage is a few micrometer, and the thickness change due to ECS is also several micrometer. The *z* direction movement generates the movement of the beam on the optical target at a similar level to the z direction movement amount, unlike the slope change. Therefore, the *z* displacement effect is negligible.

Since the rigid-body motion does not change the shape of the specimen, the induced-beam movement is virtually the same for all beams. In the equation, the beam movement generated by the warpage can be calculated by subtracting the beam movement generated by the rigid-body motion from the apparent beam movement. Then, the Eqn. (16) can be changed to:

$$\alpha(r) = \frac{1}{2}\left[\theta - \tan^{-1}\left\{\frac{-2Y_0 + tan\theta\left(X(r) + \frac{d(r)}{\sqrt{1+\tan^2\theta}}\right)}{r - X(r) - \frac{d(r)}{\sqrt{1+\tan^2\theta}}}\right\}\right] + \alpha^R \qquad (23)$$

where α^R is the slope generated by the rigid-body motion.

When there is a rigid-body motion, the shift of the curvature will occur like shown in Fig. 71(b). Like explained in Eqn. (23), the shift of the slope is generated by α^R. However, it does not affect the value of the curvature since the gradient of the slope remains the same. As a result, the warpage calculation will not be affected by the rigid body motion, even though it could generate changes in the beam movement.

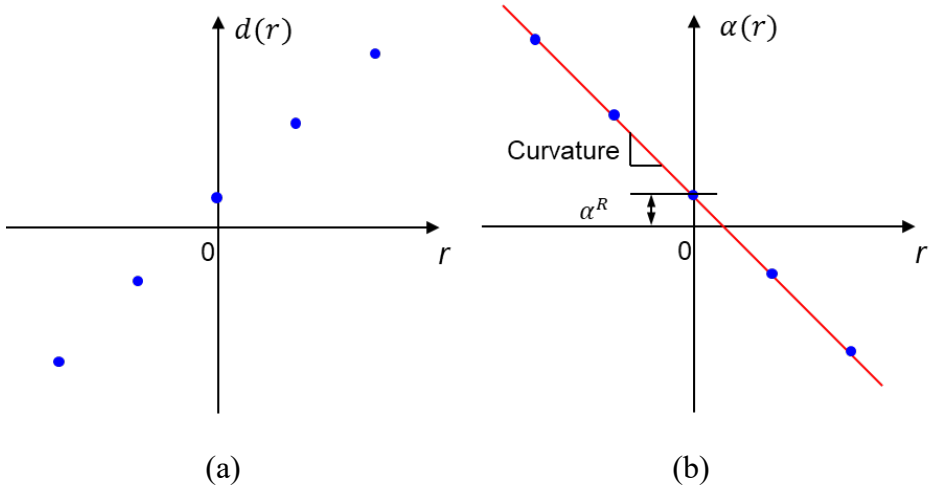

Fig. 71. The illustration of the shift of (a) the beam movement, (b) the slope and linear fitting for determining the curvature.

Chapter 4: Conclusions, Contributions, and Future Work

4.1. Conclusion

An FBG sensor was employed to measure the effective cure shrinkage of EMC. A two-stage curing process was developed to cope with technical challenges associated with the transfer mold process, in particular the high mold pressure. The effective cure shrinkage was measured under the friction-free condition by the proposed procedure while clearly identifying the gel point. The results from the repeated test confirmed the measurement repeatability of the proposed method.

The effective cure shrinkage of the EMC tested in the current study is 0.077%, which is much smaller than the shrinkage values reported in the literature. It is also significantly different from the mold shrinkage value that EMC manufactures typically provide. It is expected that the effective cure shrinkage of other EMC's with a similar filler content would be comparable.

The point-based warpage measurement technique is developed for measuring the warpage generated by the EMC transfer molding process. A novel experimental setup is designed to allow the measurement with laser beams during the molding process. The warpage of the measurement is calculated based on the movement of the reflected beam from the bimaterial EMC specimen. For the accurate tracking of the beam movement, the centroid tracking of a binarized beam method is developed. The measurement results clearly show the warpage generated during the molding process. The repeatability of the test is confirmed by the repeated warpage measurement test.

4.2. Contributions

Two important engineering quantities required for reliability assessment of encapsulated packages, which have not been measured due to the complexity involved in manufacturing processes, were measured in this thesis: (1) effective cure shrinkage (ECS) of EMC and (2) in-line warpage during molding processes. The specific technical contributions are:

(a) The effective cure shrinkage was not measured before due to the mechanical friction caused by the mold and the mold pressure. A novel two-stage measurement procedure was proposed and implemented successfully to measure the ECS of EMC without mechanical constraints. The effectiveness and the accuracy of the proposed procedure was confirmed by repeated measurements.

(b) The warpage that occurs during molding processes was required to understand how the residual stresses were developed during the processes. The existing techniques allowed measurements only after molding processes. A novel experimental technique was developed and implemented successfully to make in-line warpage measurement during the molding process.

4.3. Future work

The contributions made in this dissertation can be extended for characterizing other properties and verifying the prediction:

a) Measurement under compression molding environment

The measurement of the volume shrinkage of the EMC and the molding process induced warpage can be made under the compression molding environment. The pressure needs to be applied to the EMC continuously during the molding process. In addition to the effective cure shrinkage, the creep deformation induced by the near hydrostatic loading deformation will occur. The current warpage measurement setup allows the laser beam to be reflected from the specimen surface while the pressure is applied, but more investigation and validation is required for the measurement under pressure.

b) Verification of the warpage prediction during the transfer molding process

The warpage generated by the transfer molding process of the EMC is measured, and this can be utilized to verify the warpage prediction generated by the effective cure shrinkage of the EMC. For the warpage prediction, the cure-dependent viscoelastic properties of the EMC are required on top of the ECS during the curing process.

Reference

1. Lange, J., et al., *Residual stress build-up in thermoset films cured above their ultimate glass transition temperature.* Polymer, 1995. **36**(16): p. 3135-3141.
2. Adolf, D.B., et al., *Stresses during thermoset cure.* Journal of materials research, 1998. **13**(3): p. 530-550.
3. Sham, M.-L. and J.-K. Kim, *Evolution of residual stresses in modified epoxy resins for electronic packaging applications.* Composites Part A: Applied Science and Manufacturing, 2004. **35**(5): p. 537-546.
4. Sun, Y., et al., *Measurement of effective chemical shrinkage and equilibrium modulus of silicone elastomer used in potted electronic system.* Journal of Materials Science, 2014. **49**(24): p. 8301-8310.
5. Kim, C., et al., *Measurement of effective cure shrinkage of epoxy-based molding compound by fiber Bragg grating sensor using two-stage curing process.* Journal of Applied Polymer Science, 2022. **139**(6): p. 51620.
6. Sun, Y., H.-S. Lee, and B. Han, *Measurement of elastic properties of epoxy molding compound by single cylindrical configuration with embedded fiber Bragg grating sensor.* Experimental Mechanics, 2017. **57**(2): p. 313-324.
7. Kinet, D., et al., *Fiber Bragg grating sensors toward structural health monitoring in composite materials: Challenges and solutions.* Sensors, 2014. **14**(4): p. 7394-7419.
8. Phansalkar, S.P., et al., *Volumetric effective cure shrinkage measurement of dual curable adhesives by fiber Bragg grating sensor.* Journal of Materials Science, 2020. **55**(22): p. 9655-9664.
9. Khadka, S., J. Hoffman, and M. Kumosa, *FBG monitoring of curing in single fiber polymer composites.* Composites Science and Technology, 2020. **198**: p. 108308.
10. Wang, Y., L. Woodworth, and B. Han, *Simultaneous measurement of effective chemical shrinkage and modulus evolutions during polymerization.* Experimental Mechanics, 2011. **51**(7): p. 1155-1169.
11. Hoffman, J., S. Khadka, and M. Kumosa, *Determination of gel point and completion of curing in a single fiber/polymer composite.* Composites Science and Technology, 2020. **188**: p. 107997.
12. Phansalkar, S., C. Kim, and B. Han. *Why Is It Still Difficult to Make Accurate Prediction of the Warpage after Advanced Molding Processes?* in *2021 IEEE 71st Electronic Components and Technology Conference (ECTC)*. 2021. IEEE.
13. Phansalkar, S.P., C. Kim, and B. Han, *Effect of critical properties of epoxy molding compound on warpage prediction: A critical review.* Microelectronics Reliability, 2022. **130**: p. 114480.
14. Brunnbauer, M., et al. *An embedded device technology based on a molded reconfigured wafer*. in *56th Electronic Components and Technology Conference 2006*. 2006. IEEE.
15. Kurita, Y., et al. *Fan-Out Wafer-Level Packaging with highly flexible design capabilities*. in *3rd Electronics System Integration Technology Conference ESTC*. 2010. IEEE.

16. Braun, T., et al. *Through mold via technology for multi-sensor stacking*. in *2012 IEEE 14th Electronics Packaging Technology Conference (EPTC)*. 2012. IEEE.
17. Liu, C.C., et al. *High-performance integrated fan-out wafer level packaging (InFO-WLP): Technology and system integration*. in *2012 International Electron Devices Meeting*. 2012. IEEE.
18. Liu, H.-W., et al. *Warpage characterization of panel fan-out (P-FO) package*. in *2014 IEEE 64th Electronic Components and Technology Conference (ECTC)*. 2014. IEEE.
19. Takahashi, T., et al. *A new embedded die package—WFOP™*. in *Proceedings of the 5th Electronics System-integration Technology Conference (ESTC)*. 2014. IEEE.
20. Chen, J., et al., *Monitoring of temperature and cure-induced strain gradient in laminated composite plate with FBG sensors.* Composite Structures, 2020. **242**: p. 112168.
21. Colpo, F., L. Humbert, and J. Botsis, *Characterisation of residual stresses in a single fibre composite with FBG sensor.* Composites Science and Technology, 2007. **67**(9): p. 1830-1841.
22. Leng, J. and A. Asundi, *Structural health monitoring of smart composite materials by using EFPI and FBG sensors.* Sensors and Actuators A: Physical, 2003. **103**(3): p. 330-340.
23. Hill, K.O. and G. Meltz, *Fiber Bragg grating technology fundamentals and overview.* Journal of Lightwave Technology, 1997. **15**(8): p. 1263-1276.
24. Wang, Y., et al., *Integrated measurement technique for curing process-dependent mechanical properties of polymeric materials using fiber bragg grating.* Experimental Mechanics, 2008. **48**(1): p. 107-117.
25. Sun, Y., et al., *Dual-configuration fiber Bragg grating sensor technique to measure coefficients of thermal expansion and hygroscopic swelling.* Experimental Mechanics, 2014. **54**(4): p. 593-603.
26. Van Assche, G., et al., *Modulated differential scanning calorimetry: isothermal cure and vitrification of thermosetting systems.* Thermochimica acta, 1995. **268**: p. 121-142.
27. Wisanrakkit, G. and J. Gillham, *The glass transition temperature (Tg) as an index of chemical conversion for a high-Tg amine/epoxy system: chemical and diffusion-controlled reaction kinetics.* Journal of Applied Polymer Science, 1990. **41**(11-12): p. 2885-2929.
28. Gillham, J.K., *Formation and properties of thermosetting and high Tg polymeric materials.* Polymer Engineering & Science, 1986. **26**(20): p. 1429-1433.
29. Schawe, J., *A description of chemical and diffusion control in isothermal kinetics of cure kinetics.* Thermochimica Acta, 2002. **388**(1-2): p. 299-312.
30. Lee, D.E., et al., *A study on the curing kinetics of epoxy molding compounds with various latent catalysts using differential scanning calorimetry.* Journal of Applied Polymer Science, 2017. **134**(35): p. 45252.

31. Kim, C., et al. *On Curing-Induced Residual Stresses After Molding Processes: Mold Shrinkage, Chemical Shrinkage or Both?* in *2019 IEEE 69th Electronic Components and Technology Conference (ECTC)*. 2019. IEEE.
32. Kang, S. and I.C. Ume, *Techniques for Measuring Warpage of Chip Packages, PWBs, and PWB Assemblies.* IEEE Transactions on Components, Packaging and Manufacturing Technology, 2013. **3**(9): p. 1533-1544.
33. Han, B., *Thermal stresses in microelectronics subassemblies: quantitative characterization using photomechanics methods.* Journal of Thermal Stresses, 2003. **26**(6): p. 583-613.
34. Post, D., B. Han, and P. Ifju, *High sensitivity moiré: experimental analysis for mechanics and materials*. 1997: Springer Science & Business Media.
35. Han, C.-W. and B. Han, *High sensitivity shadow moiré using nonzero-order Talbot distance.* Experimental mechanics, 2006. **46**(4): p. 543-554.
36. Niu, Y., et al., *A comprehensive solution for electronic packages' reliability assessment with digital image correlation (DIC) method.* Microelectronics Reliability, 2018. **87**: p. 81-88.
37. Lee, M., et al., *3-D measurement system for use in microelectronics.* Advanced Packaging, 2003. **12**(11): p. 33-34.
38. Reu, P.L. and T.J. Miller, *The application of high-speed digital image correlation.* The Journal of Strain Analysis for Engineering Design, 2008. **43**(8): p. 673-688.
39. Shishido, N., et al. *Strain measurement in the microstructure of advanced electronic packages using digital image correlation*. in *2005 International Symposium on Electronics Materials and Packaging*. 2005. IEEE.
40. Du, Y., J.-H. Zhao, and P. Ho, *An optical method for measuring the two-dimensional surface curvatures of electronic packages during thermal cycling.* J. Electron. Packag., 2001. **123**(3): p. 196-199.
41. Gilardi, E., et al., *Real-time monitoring of stress evolution during thin film growth by in situ substrate curvature measurement.* Journal of Applied Physics, 2019. **125**(8): p. 082513.
42. Tsai, M. and J. Morton, *The stresses in a thermally loaded bimaterial interface.* International journal of solids and structures, 1991. **28**(8): p. 1053-1075.
43. Vaughan, M., *The Fabry-Perot interferometer: history, theory, practice and applications*. 2017: Routledge.
44. Hecht, J., *The laser guidebook*. 1999: McGraw-Hill.
45. Tong, W., *An evaluation of digital image correlation criteria for strain mapping applications.* Strain, 2005. **41**(4): p. 167-175.
46. Pan, B., et al., *Two-dimensional digital image correlation for in-plane displacement and strain measurement: a review.* Measurement science and technology, 2009. **20**(6): p. 062001.
47. Krig, S., *Computer vision metrics: Survey, taxonomy, and analysis*. 2014: Springer nature.